CDDpress

www.nature.com/cdd

ARTICLE OPEN

Check for updates

Fatal cytokine release syndrome by an aberrant FLIP/STAT3 axis

Chiara Musiu[1,15], Simone Caligola[1,15], Alessandra Fiore[1,2,15], Alessia Lamolinara[3], Cristina Frusteri[1], Francesco Domenico Del Pizzo[3], Francesco De Sanctis[1], Stefania Canè[1], Annalisa Adamo[1], Francesca Hofer[1], Roza Maria Barouni[1], Andrea Grilli[4], Serena Zilio[5], Paolo Serafini[5], Evelina Tacconelli[6], Katia Donadello[7], Leonardo Gottin[7], Enrico Polati[7], Domenico Girelli[8], Ildo Polidoro[9], Piera Amelia Iezzi[9], Domenico Angelucci[10], Andrea Capece[10], Ying Chen[11,12], Zheng-Li Shi[11], Peter J. Murray[2], Marco Chilosi[13], Ido Amit[14], Silvio Bicciato[4], Manuela Iezzi[3], Vincenzo Bronte[1,16]✉ and Stefano Ugel[1,16]✉

Inflammatory responses rapidly detect pathogen invasion and mount a regulated reaction. However, dysregulated anti-pathogen immune responses can provoke life-threatening inflammatory pathologies collectively known as cytokine release syndrome (CRS), exemplified by key clinical phenotypes unearthed during the SARS-CoV-2 pandemic. The underlying pathophysiology of CRS remains elusive. We found that FLIP, a protein that controls caspase-8 death pathways, was highly expressed in myeloid cells of COVID-19 lungs. FLIP controlled CRS by fueling a STAT3-dependent inflammatory program. Indeed, constitutive expression of a viral FLIP homolog in myeloid cells triggered a STAT3-linked, progressive, and fatal inflammatory syndrome in mice, characterized by elevated cytokine output, lymphopenia, lung injury, and multiple organ dysfunctions that mimicked human CRS. As STAT3-targeting approaches relieved inflammation, immune disorders, and organ failures in these mice, targeted intervention towards this pathway could suppress the lethal CRS inflammatory state.

Cell Death & Differentiation; https://doi.org/10.1038/s41418-021-00866-0

INTRODUCTION

Host responses to pathogens are ordered, time-dependent, and tissue-compartmentalized, coordinated by the release of soluble factors, such as growth factors and inflammatory cytokines, which engage, activate, and regulate innate immune cells [1]. Since the magnitude of the immune response is generally consistent with the pathogen load and restrained to the invasion area, cytokines with short half-life have a limited action at sites of inflammation and favor the local activation of immune cells. However, persistent infections or an uncontrolled microbial burden can prompt higher output of cytokines, which fuel emergency hematopoiesis to mobilize an increased number of leukocytes from the bone marrow and thus counterbalance the myeloid cell depletion in periphery [2]. Under these circumstances, the increase in cytokines beyond the normal thresholds can cause a catastrophic cytokine storm known as cytokine release syndrome (CRS), which eventually leads to multiple organ failures [3]. This systemic pathology is not only associated with disseminated bacterial or viral infections [4, 5] but also induced by cancer immunotherapy, i.e., chimeric antigen receptor (CAR) T cells infusion or antibody-based therapy [6–10], stem cell transplantation settings [11], as well as linked to either autoimmune or genetic disorders [12, 13]. Patients with CRS frequently display respiratory symptoms including tachypnea that progress to acute respiratory distress syndrome (ARDS) [14], severe kidney injury, hepatobiliary damage, cardiomyopathy, and neurological dysfunctions [3].

Accumulating evidence suggests a close relationship between CRS and the pandemic of coronavirus disease 2019 (COVID-19) induced by severe acute respiratory syndrome coronavirus 2 (SARS-CoV-2) [15–17]. Indeed, pathophysiological features of severe COVID-19 patients were often associated with pulmonary involvement that can require invasive mechanical ventilation in intensive care units (ICU) [18–21]. After virus entry, SARS-CoV-2 induces endothelial cell damage, complement activation, thrombin production, and fibrinolysis inhibition that result in pulmonary intravascular coagulation, vascular microthrombi formation, and, ultimately, severe vasculopathy, acute myocardial infarction, and stroke [22, 23]. Moreover, several studies have reported SARS-CoV-2 organotropism in myocardial, renal, neural, and gastrointestinal tissues, confirming COVID-19 as a complex pathology with multiple manifestations [24]. These multi-organ damages may

[1]Immunology Section, Department of Medicine, University and Hospital Trust of Verona, Verona, Italy. [2]Max Planck Institute of Biochemistry, Martinsried, Planegg, Germany. [3]CAST - Center for Advanced Studies and Technology, Department of Neurosciences Imaging and Clinical Sciences, University of G. D'Annunzio of Chieti-Pescara, Chieti, Italy. [4]Department of Life Sciences, University of Modena and Reggio Emilia, Modena, Italy. [5]Department of Microbiology and Immunology, Miller School of Medicine, University of Miami, Miami, FL, USA. [6]Division of Infectious Diseases, Department of Diagnostics and Public Health, University and Hospital Trust of Verona, Verona, Italy. [7]Intensive Care Unit, Department of Surgery, Dentistry, Maternity and Infant, University and Hospital Trust of Verona, Verona, Italy. [8]Division of Internal Medicine, Department of Medicine, University and Hospital Trust of Verona, Verona, Italy. [9]Complex Operational Unit of Forensic Medicine, Local Health Authority of Pescara, Pescara, Italy. [10]Pathological Anatomy Unit, Local Health Authority of Lanciano-Vasto-Chieti, Vasto, Italy. [11]CAS Key Laboratory of Special Pathogens, Wuhan Institute of Virology, Center for Biosafety Mega-Science, Chinese Academy of Sciences, Wuhan, Hubei, People's Republic of China. [12]University of Chinese Academy of Sciences, Beijing, People's Republic of China. [13]Department of Pathology, Pederzoli Hospital, Peschiera del Garda, Italy. [14]Department of Immunology, Weizmann Institute of Science, Rehovot, Israel. [15]These authors contributed equally: Chiara Musiu, Simone Caligola, Alessandra Fiore. [16]These authors jointly supervised this work: Vincenzo Bronte, Stefano Ugel. ✉email: vincenzo.bronte@univr.it; stefano.ugel@univr.it

Edited by Y. Shi

Received: 6 May 2021 Revised: 30 August 2021 Accepted: 31 August 2021
Published online: 13 September 2021

be associated to either direct viral toxicity or virus-dependent dysregulation of the immune system [25–30]. Thus, activation of innate immune system can be considered the main hallmark of SARS-CoV-2-associated CRS, as recently reviewed [31]. Indeed, myeloid cells are actively involved in the establishment of acute lymphopenia, microvascular dysfunctions, and organ failure, all key features of COVID-19-associated CRS [27, 32–34]. To date, however, a molecular understanding of the SARS-CoV-2-dependent myeloid cell reprogramming remains elusive.

We previously identified the anti-apoptotic cellular and viral FLICE (FADD-like IL-1β-converting enzyme)-like inhibitory proteins (hereafter c-FLIP and v-FLIP, respectively) as a factor able to reprogram monocytes [35]. FLIP isoforms are conventionally described to control cell survival and proliferation as caspase-8 inhibitors and/or NF-κB activators [36–40]. However, FLIPs regulate different biological processes based on their protein structure (e.g., the presence of death effector domains in tandem) [41] or cellular localization (e.g., trafficking between the nucleus and cytoplasm) [42, 43]. The upregulation of FLIP proteins in monocytes promoted the acquisition of unconventional phenotype characterized by the concurrent expression of immunosuppressive (e.g., programmed death-ligand 1 (PD-L1), interleukin (IL)-10) and pro-inflammatory (e.g., IL-1β, IL-6, tumor necrosis factor (TNF)-α) features, which partially depended on the nuclear translocation of the complex FLIP/nuclear factor kappa B p50 (NF-κB p50) protein [35]. In transgenic ROSA26.vFLIP;LyzM-CRE mice, where Kaposi's sarcoma virus vFLIP expression is enforced in myeloid cells, a severe and lethal inflammatory pathology developed, resembling Kaposi sarcoma-associated herpesvirus inflammatory cytokine syndrome [35].

We suspected FLIP- and pSTAT3-expressing myeloid cells were linked to COVID-19-associated CRS since their accumulation was shared by both human (h)ACE2-expressing transgenic mice and patients infected by SARS-CoV-2. Moreover, monocytes isolated from COVID-19 patients showed high myeloid expression of c-FLIP and pSTAT3 that correlated with their immunosuppressive properties. We established that vFLIP transgenic mice mirror both the immune dysfunctions and the bronchoalveolar immune landscape of patients affected by severe COVID-19. We used this unique model to assess both systemic and myeloid-targeted STAT3 interference approaches to resolve uncontrolled inflammation and acute disease manifestations.

MATERIALS/SUBJECTS AND METHODS

Mice

All genetically transgenic mice and their respective controls were gender and age-matched (typically 3–10 weeks) and both males and females were used in this study. Mice were assigned randomly to experimental groups. C57BL/6 (H-2^b) mice were originally purchased from Charles River Laboratories Inc., CD45.1^+ congenic mice (H-2^b, *B6.SJL-Ptrc^{a}Pepc^b/BoyJ*) and LySM-CRE mice (H-2^b, *B6.129P2-Lyz2$^{tm1(cre)Ifo}$/J*) were purchased from Jackson Laboratories; Rosa26.vFLIP (H-2^b) mice were a gift from Dr. Ethel Cesarman (Weill Cornell Medicine, NY, USA). All mice were maintained under specific pathogen-free conditions in the animal facility of the University of Verona. Food and water were provided ad libitum. Animal experiments were performed according to national (protocol number C46F4.26 approved by the Ministerial Decree Number 993/2020-PR of July 24, 2020 [PI: Stefano Ugel] and protocol number C46F4.8 approved by the Ministerial Decree Number 207/2018-PR of February 21, 2018 [PI: Vincenzo Bronte]) and European laws and regulations. All animal experiments were approved by Verona University Ethical Committee and conducted according to the guidelines of Federation of European Laboratory Animal Science Association (FELASA). All animal experiments were in accordance with the Amsterdam Protocol on animal protection and welfare: mice were monitored daily and euthanized when displaying excessive discomfort.

Ethics and acquirement of human samples

All 48 patients with COVID-19 and 4 healthy donors in this study were admitted, within the period from March 12th to April 20th 2020 to the University Hospital of Verona or Hospital of Pescara. At sampling, the stage of disease was categorized as mild (patients not requiring non-invasive/mechanical ventilation and/or admission to ICU) or severe (patients requiring admission to ICU and/or non-invasive/mechanical ventilation).

For immunohistochemistry (IHC) analysis of lung autopsy, this study includes a group of 4 non-respiratory disease (NRD) patients, 4 bacterial pneumonia (BP) patients, and 23 COVID-19 patients. The clinical features are recapitulated in Table 1 and Table 2A, B.

For molecular data (i.e., single-cell transcriptomic analysis), phenotypic analysis (myeloid characterization in terms of expression of immune suppression hallmarks), and functional data (myeloid immune-suppressive assay), this study includes a group of 14 severe COVID-19 patients admitted to ICU, 11 mild SARS-CoV-2 patients, and 4 HDs. The clinical features of the 3 groups of subjects are recapitulated in Supplementary information, Table 2C.

All the patients (and/or initially their families) provided written informed consent before sampling and for the use of their clinical and biological data. This study was approved by the local ethical committee (protocol 17963; PI: Vincenzo Bronte; ClinicalTrials.gov identifier NCT04438629). All clinical investigations were conducted according to Declaration of Helsinki principles, and informed consent was obtained from all study participants.

Detection of cytokines and serology

ProcartaPlex Mouse Cytokine & Chemokine Panel 1A (36 plex: IFN-γ; IL-12p70; IL-13; IL-1β; IL-2; IL-4; IL-5; IL-6; TNF-α; GM-CSF; IL-18; IL-10; IL-17A; IL-22; IL-23; IL-27; IL-9; GRO-α; IP-10; MCP-1; MCP-3; MIP-1α; MIP-1β; MIP-2; RANTES; Eotaxin; IFNα; IL-15/IL-15R; IL-28; IL-31; IL-1α; IL-3; G-CSF; LIF; ENA-78/CXCL5; M-CSF) (eBioscience, Thermo Fisher Scientific, Waltham, MA, USA) and Cytokine 25-Plex Human ProcartaPlex™ Panel 1B (25 plex: GM-CSF, IFN gamma, IL-1β, IL-2, IL-4, IL-5, IL-6, IL-12p70, IL-13, IL-18, TNF α, IL-9, IL-10, IL-17A (CTLA-8), IL-21, IL-22, IL-23, IL-27, IFN-α, IL-1 α, IL-1RA, IL-7, IL- 15, IL-31, TNFβ (eBioscience, Thermo Fisher Scientific, Waltham, MA, USA) were performed according to manufacturer's instructions.

Flow cytometry

In total, $0.5–2 \times 10^6$ cells were washed in PBS and incubated with FcReceptor Blocking reagent CD16/32 (Biolegend) or FcReceptor Blocking reagent (Miltenyi Biotec) in staining buffer (2% FBS in PBS) for 10 min at 4 °C to saturate FcR. The following mAbs were then used for cell labeling: anti-mouse CD3 (17A2), CD45.1 (A20), CD11b (M1/70), B220 (RA3-6B2), CD45.2 (104), Ly6G (1A8), Ly6C (HK1.4), FOXP3 (NRRF-30), CD3ξ (145-2C11), CD25 (PC61.5), CD62L (MEL-14), CD8a (53-6.7), CD4 (RM4-5), LAG-3 (C9B7W), TIM-3 (B8.2C12), PD1 (29F.1A12), p-STAT3 (Ser727) (D4X3C), NK1.1 (PK136) or anti-mouse/human CD44 (IM7), p-STAT3 (pTyr705) (LUVNKLA) or human CD16 (3G8), CD3 (UCHT1), HLA-DR (L243), CD14 (MφP9), PD-L1 (MIH1), and Aqua LIVE/DEAD dye. All antibodies were purchased from the following companies: BD Biosciences (San Jose, CA, USA), eBiosciences (Thermo Fisher Scientific, Waltham, MA, USA), Biolegend (San Diego, CA, USA), and Cell Signaling Technologies (Danvers, MA, USA). Extracellular antigens were stained for 30 min at 4 °C in staining buffer. For cytokines and transcriptional factor analysis, cells were fixed and permeabilized with Foxp3/Transcription Factor Staining Buffer Set (eBioscience) following manufacturer instructions. Intracellular antigens were stained for 1 h in the appropriate 1x Perm/Wash buffer. Samples were acquired with a FACSCanto II (BD, Franklin Lakes, NJ, USA) and analyzed with FlowJo software (Treestar Inc.).

To determine the intracellular levels of p-STAT3 (Tyr705) using clone LUVNKLA, after surface markers staining, cells were fixed with 2% paraformaldehyde (Sigma-Aldrich) and permeabilized with 90% cold methanol. All steps were performed in ice.

Table 1. Main histopathological data of the study population.

Parameters	Total ($N = 23$)
Airways	
Tracheobronchial inflammation, *n* (%)	
Acute, diffuse	1 (4.3%)
Acute, focal	1 (4.3%)
Chronic, diffuse	0
Chronic, focal	1 (4.3%)
Not available	20 (87.1%)
Alveolar space	
Acute inflammation, *n* (%)	
Present, diffuse	1 (4.3%)
Present, focal	5 (21.7%)
Absent	17 (74%)
Chronic inflammation, *n* (%)	
Present, diffuse	1 (4.3%)
Present, focal	8 (34.8%)
Absent	14 (60.9%)
Hyaline membrane, *n* (%)	
Present, diffuse	6 (26.1%)
Present, focal	1 (4.3%)
Absent	16 (69.6%)
Pneumocyte type II hyperplasia, *n* (%)	
Present, diffuse	2 (8.7%)
Present, focal	1 (4.3%)
Absent	20 (87%)
Alveolar wall	
Chronic inflammation, *n* (%)	
Present, diffuse	4 (17.4%)
Present, focal	15 (62.2%)
Absent	4 (17.4%)
Fibrosis, *n* (%)	
Present, focal	11 (47.8%)
Present, diffuse	9 (39.1%)
Absent	3 (13.1%)
Vessels, *n* (%)	
Vessel congestion	7 (30.4%)
Blood extravasation	6 (26.1%)
Microthrombi	1 (4.3%)
Large thrombi	3 (13%)
Other lesions, n (%)	
Succular emphysema	6 (26.1%)
Calcifications	2 (8.7%)
Anthracosis	3 (13%)
Myofibroblastic foci	2 (8.7%)

Table 2. Main clinical data of: (A) patients for IHC analysis of lung autopsy, (B) COVID-19 patients for IHC analysis of lung autopsy, and (C) patients for molecular, phenotypic, and functional data.

	NRD	BP	COVID-19
(A) Main clinical data of patients for IHC analysis of lung autopsy			
Parameters	$N = 4$	$N = 4$	$N = 23$
Age (year), median (range)	64.5 (48–80)	63 (44–82)	82 (54–95)
Gender, *n* (%)			
Males	2 (50%)	4 (100%)	11 (48%)
Females	2 (50%)		12 (52%)
Co-morbidity, *n* (%)			
Absent	0	1 (25%)	3 (13%)
1	1 (25%)	2 (50%)	8 (34.8%)
2	0	1 (25%)	8 (34.8%)
3	3 (75%)	0	4 (17.4%)
(B) Main clinical data of COVID-19 patients for IHC analysis of lung autopsy			
		c-FLIP$^-$CD68$^-$pSTAT3$^-$	c-FLIP$^+$CD68$^+$pSTAT3$^+$
Days of hospitalization, median (range)		25 (11–52); $N = 10$	18 (0–32); $N = 13$
CRP (mg/L), median (range)		75.79 (9–271.2); $N = 10$	80.83 (5.92–242.5); $N = 12$
Pro-calcitonin (ng/mL), median (range)		2.12 (0.14–9.45); $N = 9$	0.81 (0.2–9.45); $N = 10$
(C) Main clinical data of patients for molecular, phenotypic, and functional data			
	Healthy controls	Mild patients	Severe patients
Characteristics	$N = 4$	$N = 11$	$N = 14$
Anagraphic			
Age, Yr: Median (IQR)	66 (64–73)	71 (63–86)	70 (60–71)
Male, no. (%)	3 (75)	10 (90.9)	6 (85.7)
Clinical features at sampling			
APACHE score, median (IQR)	–	–	25 (13.5–28)
SOFA score, median (IQR)	–	–	7 (4–8)
Score on ordinal scale (1–8), median (IQR)	–	4 (3–4)	5 (3–7)

FLIP protein expression was evaluated by flow cytometry by indirect amplification on intracellular signal. In details, after surface markers staining, 1×10^6 PBMCs were fixed and permeabilized with Foxp3/Transcription Factor Staining Buffer Set (eBioscience). Before the intracellular staining, cells were incubated with FcReceptor Blocking reagent (Miltenyi Biotec) for 10 min at RT in the appropriate 1x Perm/Wash buffer. Rabbit anti-FLIP antibody (D5J1E; 1:100; Cell Signaling Technologies) was added for 2 h at 4 °C. Signal was amplified with a secondary anti-rabbit IgG (H + L) (#8885, Cell Signaling Technology) for 30 min at 4 °C. To normalize the expression level between the analyzed samples we applied the following formula: Normalized MFI = (MFI sample − MFI FMO)/MFI FMO.

Generation of vFLIP-chimera mice

To generate the vFLIP-chimera mouse model, C57BL/6 female of 8 weeks of age received 9 Gy total body irradiation (TBI) using ^{137}Cs-source irradiator. Six hours after pre-conditioning, irradiated recipient mice were intravenously injected with 5×10^6 bone marrow cells obtained from CD45.1 WT and ROSAvFLIP Tg (CD45.2) donor mice at different ratio (vFLIP/WT ratio 0/1; 1/1; 3/1; 1/0). Bone marrow cells over-expressing FLIP protein from Kaposi's sarcoma virus (v-FLIP) in myeloid compartment were collected from ROSA26.vFLIP Tg knock-in mice. These mice were obtained by crossing ROSA26.vFLIP knock-in mice with mice expressing Cre recombinase under control of the endogenous *Lyz2* promoter. For the therapeutic studies, 50% WT-50% vFLIP ratio was used to generate the vFLIP-chimera mice. Four weeks post bone-marrow transplantation, peripheral blood of recipient mice was analyzed for the presence of donor-derived cells.

Human cell isolation and functional assay

Cells were isolated from EDTA-treated tubes (BD Biosciences, NJ, USA) and freshly separated by Ficoll-Hypaque (GE Healthcare) gradient centrifugation. PBMCs were counted and the monocyte fraction (CD14$^+$) was further isolated by CD14-microbeads (Miltenyi Biotec), following manufacturer's instructions. The purity of the CD14$^+$ fraction was evaluated by flow cytometry analysis. Samples with a purity >95% were assessed for their suppressive capacity. CD14$^+$ cells were collected and cultured with 1 μM CellTrace (Thermo Fisher Scientific) labeled PBMCs, stimulated with coated anti-CD3 (OKT-3) and soluble anti-CD28 (28.2) for 4 days in 37 °C and 8% CO_2 incubator. For the cells, a ratio of 3:1 (target:effector) was used. At the end of the culture, cells were

stained with anti-CD3 (UCHT1) and CellTrace signal of lymphocytes. Samples were acquired with FACS-Canto II (BD, Franklin Lakes, NJ, USA) using TruCountTM tubes (BD, Franklin Lakes, NJ, USA) to determine the absolute cell number of $CD3^+$ cells in the samples. Data were analyzed by FlowJo software (Tree Star, Inc., Ashland, OR, USA).

Cytokines released by patients' monocytes were quantified by Human ProcartaPlex™ Panel 1 multiplex. Samples with a purity >95% were assessed for their cytokine production. Briefly, 5×10^5 $CD14^+$ cells were plated in 24-well plates for 12 h. At the end of the incubation, viability was evaluated by flow cytometry.

Immunofluorescence (IF) and immunohistochemistry (IHC)

To determinate the presence of pSTAT3 Tyr705 and c-FLIP in human samples, $CD14^+$ cells were plated on coverslips (ibidi GmbH; Cat#80826), fixed in 4% formaldehyde for 10 min at RT, and blocked with 0.1% Triton X-100 in PBS 1x for 10 min at RT. To detect the intracellular signal, permeabilization was performed in 0.1% Triton X-100 in PBS 1x and 20% of normal goat serum (Vector Laboratories) for 2 h at RT. Primary mAbs rabbit anti-FLIP antibody (D5J1E; 1:100; Cell Signaling Technologies) and mouse anti-pSTAT3 (Try705) (LUVNKLA; 1:50; Invitrogen) were diluted in PBS 1x supplemented with 0.05% Tween-20 (Biorad, Cat#1706531) solution over-night at 4 °C. Signal was amplified with secondary antibodies goat anti-rabbit IgG Alexa Fluor 488 (1:1000; CAT#A11034; Invitrogen) and donkey anti-mouse IgG Alexa Fluor 647 (1:1000; Cat#A-31571 Invitrogen) in 0.1% Triton X-100 in PBS 1x and 20% of normal goat serum for 1 h at RT followed by nuclei staining with Hoechst 33342 (H1399; 1:500; Invitrogen) in PBS 1x for 10 min at RT.

Tissues were fixed in 10% neutral buffered formalin and embedded in paraffin; after embedding, 5-µm-thick sections were cut and stained with Hematoxylin and Eosin (Bio-Optica, Italy) for histological examination. For immunohistochemical and immunofluorescence analysis of samples, slides were deparaffinized, serially rehydrated and, after the appropriate antigen retrieval procedure, incubated with the following primary antibodies: rabbit anti-mouse pSTAT3 antibody (#9145, Cell Signaling), rat anti-mouse B220 antibody (550286, BD Pharmigen), mouse anti-human CD68 antibody (M0814, Dako), mouse anti-Human/Mouse/Rat FLIP antibody (MAB8430, R&D), rabbit anti-mouse CD3 antibody (ab16669, Abcam), rabbit anti-mouse F4/80 antibody (#70076, Cell Signaling), rabbit anti-mouse CD62P antibody (ab255822, Abcam), rabbit anti-mouse Neutrophil Elastase antibody (ab68672, Abcam), rabbit anti-mouse CD4 antibody (#25229, Cell Signaling), and rat anti-mouse Foxp3 antibody (14-5773-82, eBioscience), followed by the appropriate secondary antibodies. Immunostainings were developed with streptavidin peroxidase methods and the DAB Chromogen system (Dako). After chromogen incubation, slides were counterstained in Hematoxylin (Bio-Optica) and images were acquired by Leica DMRD optical microscope (Leica). For immunofluorescence, immunostainings were developed using TSA Plus Cyanine 3, TSA Plus Cyanine 5, or TSA Plus Fluorescein Systems (NEL744001KT, NEL745001KT, or NEL741001KT, respectively, Akoya Biosciences), goat anti-rabbit Alexa Fluor 488 (A11008, ThermoFisher), goat anti-rat Alexa Fluor 546 (A11081, ThermoFisher), goat anti-mouse Alexa Fluor Plus 647 (A32728, ThermoFisher), and nuclei were stained with Dapi (Sigma). Images were acquired by Zeiss LSM800 confocal microscope.

For histological assessment of collagen deposition, trichrome staining was performed using the Masson Trichrome with Aniline Blue Staining Kit (04-010802, Bio-Optica). Pathological score was independently evaluated by two pathologists in double-blind using the standard guideline previously published [44].

The percentage of CD3, B220, or F4-80 positive cells was evaluated on digital images of total reconstructed spleen section (5–10 ×50 microscopic fields per sample); clear brown positive cells were selected with the Magic Wand Tool of Adobe Photoshop. For each spleen, the number of positive cell pixels indicated in the histogram window was reported as % on the number of total spleen area (expressed in pixel). The number of Foxp3 positive cells was evaluated on digital images of immunofluorescence section as percentage on CD4 positive cells.

Western blotting (WB)

Cell lysates of purified circulating $CD14^+$ cells were made in RIPA buffer with the addition of protease inhibitor cocktail tablets (Roche, Monza, Italy) and sodium vanadate. Insoluble material was removed by centrifugation. Samples were subjected to SDS-polyacrylamide 10% Bis-Tris gel electrophoresis and blotted onto PVDF-membrane (Immobilon P membranes, Millipore, Billerica, MA, USA). Tris-buffered saline plus 0.05% Tween-20 and 5% non-fat milk were used to block unspecific sites. Membranes were blocked in Tris-buffered saline plus 0.05% Tween-20 and 5% non-fat milk. Membranes were incubated with anti-FLIP (D5J1E) purchased from Cell Signaling Technologies (Danvers, MA, USA), followed by incubation with the secondary goat anti-rabbit IgG antibody, horseradish peroxidase (HRP)-conjugated (Millipore, Billerica, MA, USA). HRP-conjugated anti-β actin (Cell Signaling Technologies, Danvers, MA, USA) was used as reference. Proteins were revealed by GE ImageQuant LAS400 with Pico substrate (ThermoFisher Scientific, Waltham, MA, USA).

In vivo STAT3 targeting

The in vivo effect of drugs treatment was investigated in the vFLIP-chimera mouse model, 4 weeks after the bone marrow cells transplantation. Chimera mice that displayed at least 20% of donor-derived cells were randomized before beginning treatment. Chimera mice were treated using 8 intraperitoneal administrations of Baricitinib (10 mg/kg; Cayman chemicals) or Silibinin (100 mg/kg; Sigma-Aldrich) every 2 days, for a total of 9 treatments. shRNA treatments were performed three times a week by injecting shRNA (anti-STAT3 or scramble) loaded onto 4PD intravenously as previously described [45], for a total of 9 treatments. shRNA STAT3 sequence: 5′-UAAUACGACUCACUAUAAGGAGGGUGUCA GAUCACAUGGGCUUUCAAGAGAUCUCAACGGACCAUGCUACUGCC UU-3′; shRNA scramble STAT3 sequence: 5′-UAAUACGACUCA CUAUAAGGGCAGUAGCAUGGUCCGUUGAGAUUCAAGAGAUCUCA ACGGACCAUGCUACUGCCUU-3′ (Boston Open Labs). IHC and flow cytometry analysis were performed at the end of the experiment (2 weeks after the first treatment). Chimera mice were euthanized when the weight loss reached 20% of body-weight as an animal protocol-defined endpoint.

Preparation of cell suspensions from organs

Mice were euthanized by CO_2 inhalation. For lung flow cytometry analysis, mice were immediately perfused with 20 mL ice-cold PBS. Organs were harvested and processed as follows. Spleens were mechanically disaggregated and filtered (Corning Inc). Lungs were cut in small pieces with scissors, enzymatically digested at 37 °C for 45 min with a solution containing collagenase IV (1 mg/ml), hyaluronidase (0.1 mg/ml), and DNase (4.5 mg/ml) (Sigma-Aldrich). For bone marrow, tibias and femurs were flushed in RPMI 1640 (Euroclone) supplemented with 10% heat-inactivated FBS (Superior, Merck), 2 mM L-glutamine, 10 mM HEPES, 1 mM sodium pyruvate, 150 U/mL streptomycin, 200 U/mL penicillin/streptomycin (all from Euroclone). Cells were then collected, filtered and red blood cells were lysed at RT for 5 min with ACK Lysing Buffer (Lonza). Peripheral blood was washed with PBS and red blood cells were lysed twice at RT for 10 min. Single-cell suspensions were then analyzed by flow cytometry.

Single-cell RNA sequencing (scRNA-seq)

Lung pooled from 3 untreated-chimera, 3 silibinin-treated, 3 baricitinib-treated, and 3 vFLIP-tg mice were digested as described

in "Preparation of cell suspensions from organs" section. Single-cell suspension (10^4 cells) was loaded on a GemCode Single Cell Instrument (10x Chromium System) to generate single-cell GEMs.

Single-cell RNA-seq data preprocessing

Raw bcl files were demultiplexed using bcl2fastq v2.20 from Illumina and processed using 10x Cell Ranger v3.1.0. In particular, 'cellranger count' command with parameter '--expect-cells=4000' was used to quantify reads mapped to mouse (mm10) and human (GRCh38) genomes and to obtain the unique molecular identifier (UMI) count tables.

Single-cell RNA-seq data quality control

The quality control steps before data integration were performed individually for each sample using the R package 'Seurat' [46–48] and Scrublet [49] for removing putative doublets. In particular, to retain high-quality transcriptomes, the cells were filtered according to the following parameters: percentage of mitochondrial counts, minimum number of expressed genes, min/max number of UMIs, and doublet score. For both mouse and human only cells with <20% of total counts explained by mitochondrial genes were maintained. Scrublet thresholds were chosen seeing at the histograms of observed transcriptomes and simulated doublets as recommended by the author guidelines (https://github.com/AllonKleinLab/scrublet/blob/master/examples/scrublet_basics.ipynb). The other filtering thresholds were chosen looking at the distribution of the data in order to remove cells with a potential outlier behavior. The complete list of filtering thresholds is summarized in Dataset 2.

Single-cell RNA-seq data integration

Both for mouse and human cells all the samples were integrated using the standard Seurat v3 integration procedure [48]. Before data integration, the original count matrices were normalized using log-normalization from the Seurat package with default parameters. Next, both for mouse and human, the scRNA-seq data were integrated using the first 30 dimensions of canonical correlation analysis (CCA). After integration, count matrices were scaled regressing for the total number of genes, UMIs, and percentage of mitochondrial gene expression. Next, principal component analysis (PCA) was performed on the top 2000 most variable features obtained using the 'vst' procedure of Seurat. The top 20 principal components were used to execute t-distributed stochastic neighbor embedding (tSNE) algorithm and to project the cells into a two-dimensional space.

Cell type identification

After data integration, cell type identification, both for mouse and human, was performed using multiple reference-based cell annotation and manual inspection. For mouse, SingleR [50] with gene expression profiles from Immunological Genome Project [51] and Mouse RNA-seq [52] was used in combination with scMCA [53]. For human data, SingleR was executed using reference gene signatures from Blueprint/ENCODE [54, 55], Human primary cell atlas [56], and Monaco immune data [57]. Prior to final cell classification, cell labels were simplified in order to discard ultra-rare (<20 cells) cell annotations and harmonized to match corresponding main population labels across the different reference datasets. Final cell identity was obtained taking the classification determined by 2 out of 3 reference datasets and annotating as "Unclassified" the cells labeled differently with all the 3 datasets. Finally, manual inspection was performed to check the final annotations and to solve part of the unclassified cells looking at the expression of known marker genes through appropriate dot plots (Figure S4B and S4D). Overall, about 2% of mouse and human cells were labeled as Unclassified.

Cluster analysis of neutrophils and monocytes/macrophages

To have a better resolution in subset cluster analysis, neutrophils and monocytes/macrophages populations of both mouse and human were extracted from the dataset, re-integrated using a similar approach to above (see the "Single-cell RNA-seq data integration" section), and finally clustered. For neutrophils, cells were integrated using Seurat with 30 CCA dimensions and clustered using 10 principal components for mouse and 12 for human, respectively, to construct a shared nearest neighbor graph (SNN). A resolution of 0.12 for mouse and 0.15 for human, respectively, was used to find significant clusters (≥2% of cells) through the SNN. Monocytes/macrophages were similarly integrated and clustered using 11 and 10 principal components for mouse and human, respectively, with a resolution of 0.15. For human samples, the parameter 'k.filter=80' was set to find the Seurat integration anchors. After integration and clustering, cells were projected into a two-dimensional space using the tSNE algorithm.

Mapping between human and mouse genes

To map mouse to human gene symbols the ortholog table from the Mouse Genome Informatics (MGI, http://www.informatics.jax.org/downloads/reports/HMD_HumanPhenotype.rpt) was used keeping only the genes with a one-to-one mapping between the two species (Dataset 1).

Gene set analysis

Gene set analysis for scRNA-seq and bulk RNA-seq data was performed using 'fgsea' [58] that performs pre-ranked gene set enrichment analysis (GSEA, [59]) or with the 'gsva' R package that performs gene set variation analysis (GSVA, [60]). Gene-level statistics for scRNA-seq data used as input for GSEA were calculated using the Seurat function 'FindMarkers' with the Wilcoxon rank-sum test with average log-fold change threshold of 0 for bulk-like analyses and 0.1 for cluster-level analyses. For the analysis of bulk RNA-seq of previous published Sars-CoV-2 ACE2-transgenic mice dataset (GSE154104), gene-level statistics were obtained through DESeq2 package [61]. In particular, after removing duplicated gene symbols, differential expression analysis was performed to compare Sars-CoV-2 ACE2-transgenic mice 7 days post infection (dpi) and mock-infected mice (0 dpi) with log2-fold change different from 0. The 50 hallmark gene sets from MSigDB [62] were used as input both for GSEA and GSVA. For GSEA, only up- or downregulated gene sets with adjusted p-value <0.05 were considered statistically significant.

Reference-based classification of human BAL neutrophils

SingleR was used to label the cells of the neutrophil clusters in the human BALs using as reference the gene expression of vFLIP mice neutrophil clusters. In particular, a bulk-like mouse reference was created, taking the log-normalized average expression of each gene in each cluster, and giving it to SingleR for reference-based classification after mapping mouse genes to human gene symbols via orthology (see the "Mapping between human and mouse genes" section). SingleR was executed taking the top 100 differential expressed genes between cluster comparisons specifying the parameter 'de.n' (Dataset 1).

Data visualization

In general, the bioinformatics figures were obtained using functions of the R packages Seurat and ggplot2 [63].

Statistical analysis

All data are reported as mean ± standard error (SE) of the mean. Statistical analyses were performed using Graph Pad Prism (version 8.0.2). Student t test and Wilcoxon–Mann–Whitney test were used to determine statistical significance of differences between two treatment groups. Values were considered significant at $P \leq 0.05$.

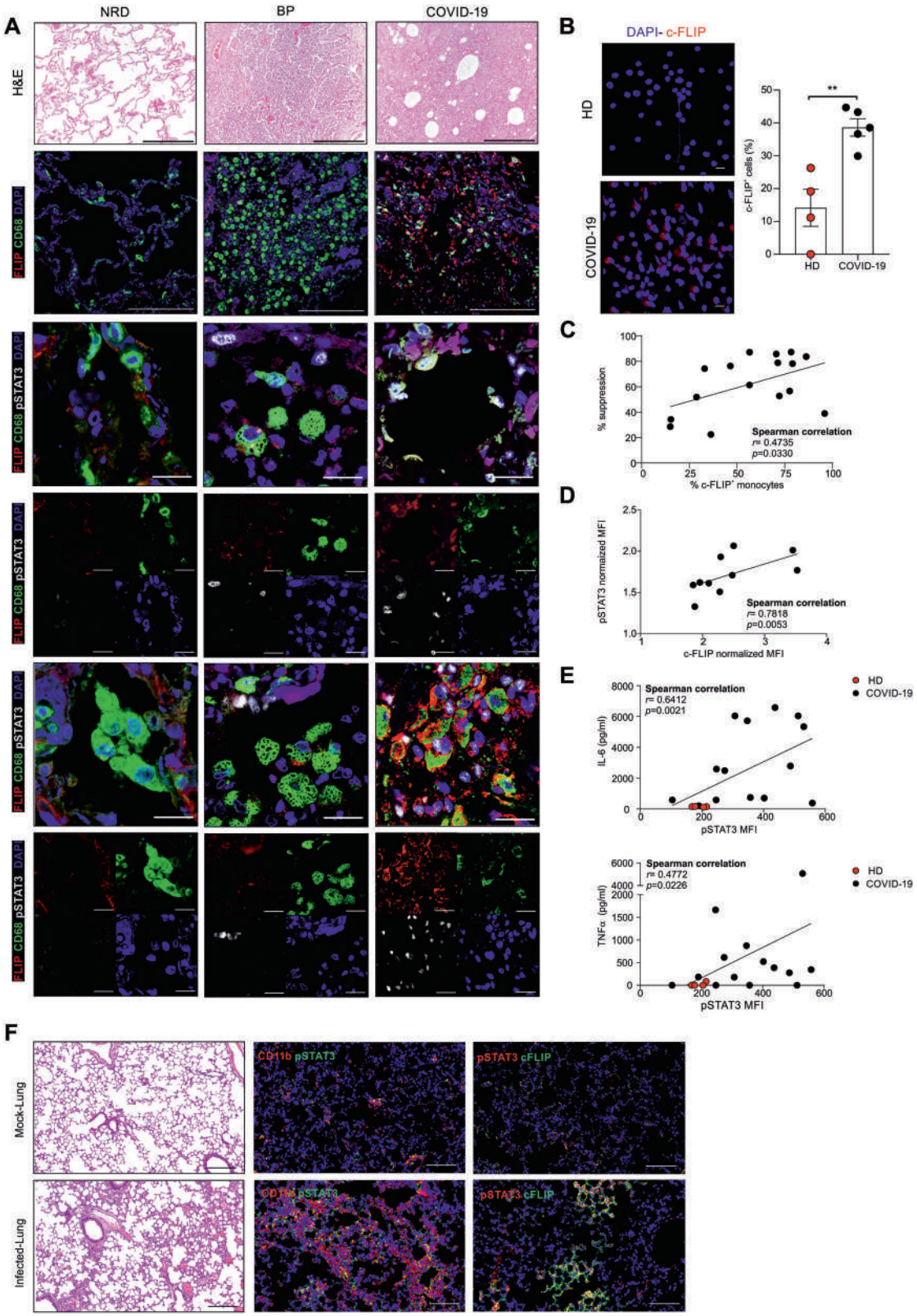

RESULTS

SARS-CoV-2 infection-induced c-FLIP overexpression in both COVID-19 patients and virus-infected, HFH4-hACE2 transgenic mice

Viruses have evolved a myriad of ways to escape host apoptotic process and thereby preserve infected cells from early death, which eliminates the replicative niche [64]. Several viruses including hepatitis C virus [65], hepatitis B virus [66], human T-cell leukemia virus-1 [67], human immunodeficiency virus 1 [68], Epstein Barr Virus [69], and influenza A virus [70] induce the anti-apoptotic protein c-FLIP, which blocks caspase-mediated cell death [40]. Poxviruses and herpesviruses encode proteins with

Fig. 1 c-FLIP and pSTAT3 expression in SARS-CoV-2-infected hosts. A Representative H&E-stained microscopy images of lung tissue of non-respiratory disease (NRD), bacterial pneumonia (BP), and COVID-19 patients (upper panel). Scale bar, 200 μm. Representative immunofluorescence (IF) staining of alveolar macrophages (second, third, and fourth lines) and histiocytic cells (fifth and sixth lines). Cells were stained for CD68 (green), c-FLIP (red), pSTAT3 (white), and DAPI (blue). Scale bar, 20 μm. **B** Quantification and representative IF staining of c-FLIP in circulating monocytes ($CD14^+$ cells) purified from healthy donors (HD, $n = 4$) or COVID-19 patients ($n = 5$). Cells were stained for DAPI (blue) and c-FLIP (red). Scale bar, 10 μm. **C** Correlation between percentage of suppression and percentage of circulating c-FLIP-expressing monocytes isolated from COVID-19 patients ($n = 16$). **D** Correlation between pSTAT3 and c-FLIP normalized expression in circulating monocytes ($CD14^+$ cells) isolated from COVID-19 patients ($n = 10$). **E** Correlation between the release of IL-6 or TNF-α cytokines and pSTAT3 expression in monocytes ($CD14^+$ cells) from HD (red, $n = 4$) and COVID-19 patients (black, $n = 13$). **F** Representative hematoxylin and eosin (H&E)-stained microscopy images of lung tissue of HFH4-hACE2 transgenic mice SARS-CoV-2-infected or mock-infected mice. Scale bar, 200 μm. pSTAT3, c-FLIP, and CD11b expression levels were detected by indirect immunofluorescence (IFA) staining. Scale bar, 100 μm. Correlation analysis was performed by Spearman's rank correlation (**C**–**E**).

high homology to c-FLIP, such as the Kaposi's herpesvirus K13/vFLIP and the herpesvirus saimiri orf71, which harbor DED domains responsible for blocking procaspase cleavage, preventing apoptosis, and favoring viral latency [36]. Thus, FLIP expression is linked to viral replication by suppressing host cell death.

To examine c-FLIP alterations in COVID-19, we analyzed lung autopsy samples from patients infected by SARS-CoV-2 (COVID-19; $n = 23$) or affected by bacterial pneumonia (BP; $n = 4$) or other diseases (NRD; $n = 4$) (Supplementary information, Table 2A). In the latter group, the respiratory tract was not altered by severe inflammation and showed a tissue structure almost devoid of pathological aspects (Fig. 1A, first line). By contrast, the histopathological features of the lungs from COVID-19 patients were showed heterogeneous inflammation and tissue damage (Supplementary information, Table 1) [22, 71]. When we evaluated the number of $CD68^+$ myeloid cells, which encompass alveolar macrophages, monocytes/interstitial macrophages, and histiocytes [72, 73], for the expression of FLIP, COVID-19 samples displayed a variable number of FLIP-expressing $CD68^+$ cells (Fig. 1A, second line) suggesting an accumulation of $FLIP^+$ myeloid cells during COVID-19 progression. Conversely, COVID-19 samples displayed also a moderate and heterogeneous infiltration of neutrophils, identified as neutrophil-elastase (NE) positive cells, which were not positive also for FLIP (Supplementary information, Fig. S1A). Previously, we found enforced FLIP expression reprogramming myeloid cells into immune regulatory elements through the aberrant activation of several molecular pathways, including STAT3-dependent signaling [35]. Since STAT3 hyperactivation was advanced as the orchestrator of most commonly COVID-19-associated features, such as rapid coagulopathy, thrombosis, tissue fibrosis, production of inflammatory cytokines and chemokines, as well as T-cell lymphopenia [74], we next evaluated the expression of pSTAT3 in the selected pathological lung fields. We detected a weak pSTAT3 expression in NRD samples, while a limited pSTAT3 pattern was restricted to stromal cells in bacterial pneumonia sections. However, consistent and diffuse expression of pSTAT3 was shared in COVID-19 samples by numerous cell types; among them, several $CD68^+FLIP^+$ alveolar macrophages (Fig. 1A, third and fourth lines), histiocytic cells (Fig. 1A, fifth and sixth lines), and monocytes/interstitial macrophages (Supplementary information, Fig. S1B). Interestingly, $CD68^+FLIP^+p\text{-}STAT3^+$ cells were present in 56.5% (13/23) of analyzed cases and their presence significantly correlated with a shorter time to fatal evolution, expressed as the number of hospitalization days (i.e., absence of $CD68^+FLIP^+pSTAT3^+$ cells ($n = 10$) 25 ± 14.4 days *vs.* presence of $CD68^+FLIP^+pSTAT3^+$ cells ($n = 13$) 18 ± 9.3 days; $p = 0.0223$) (Supplementary information, Table 2B). On the contrary, $CD68^+$ expression alone is not predictive of disease progression since it did not discriminate between patients with a shorter or a longer hospitalization time (Supplementary information, Fig. S1C).

We assessed c-FLIP and pSTAT3 expression in fresh circulating monocytes ($CD14^+$ cells) isolated from SARS-CoV-2-infected individuals (Supplementary information, Table 2C). Immunofluorescence analysis revealed an increased expression of c-FLIP in circulating $CD14^+$ cells isolated from COVID-19 patients compared to heathy donors (HDs) (Fig. 1B), together with a linear correlation between c-FLIP-expression in monocytes and their immunosuppressive properties (Fig. 1C, Supplementary information, Fig. S1D-E). PD-L1 was enhanced in c-FLIP-expressing $CD14^+$ cells (Supplementary information, Fig. S1F), in agreement with our previous findings in pancreatic ductal adenocarcinoma (PDAC) patients [35], hinting to common mechanisms of innate immunity modulation in COVID-19 and cancer.

We next sought to determine whether c-FLIP-expressing circulating monocytes exhibited concomitant activation of STAT3. We identified a significant direct correlation between pSTAT3 and c-FLIP expression in circulating $CD14^+$ cells isolated from COVID-19 patients (Fig. 1D), hinting to the aberrant activation of FLIP/STAT3 axis in myeloid cells not only at pulmonary site but also in periphery. The STAT3 pathway in myeloid cells is relevant for acquiring immunosuppressive functions [75–77] and for driving the production of cytokines during immune disorders [78], two conditions jointly cooperating to establish a severe lymphopenia, one of the signs of clinical severity in COVID-19 patients. Monocytes isolated from COVID-19 patients secreted a greater amount of cytokines, on a per-cell basis, which correlated with the pSTAT3 expression (Fig. 1E and Supplementary information, Fig. S1G), consistent with published data about the monocyte contribution to the cytokine storm [79, 80].

To establish a direct link between FLIP and pSTAT3 dysregulation following SARS-Cov-2 infection, we analyzed the lung of mice transgenic for hACE2 (HFH4-hACE2 mice) that were intranasally infected with either SARS-CoV-2 or mock virus, as previously described [81]. Examination of lung tissues 7 days after virus challenge demonstrated that SARS-CoV-2 infection induced severe pneumonia characterized by increased $CD11b^+$ myeloid cell accumulation in perivascular and alveolar locations (Fig. 1F). Of note, lung-infiltrating myeloid cells in SARS-CoV-2-infected mice expressed higher p-STAT3 levels than the control group (Fig. 1F). Moreover, we found an increased expression of p-STAT3 in $c\text{-}FLIP^+$ cells, which morphologically resemble myeloid cells, in the lung of SARS-CoV-2-infected mice (Fig. 1F) as exemplified by the presence of $p\text{-}STAT3^+c\text{-}FLIP^+CD68^+$ lung-infiltrating cells exclusively in SARS-CoV-2-infected mice (Supplementary information, Fig. S1H). Collectively, these data establish that myeloid subsets are converted into FLIP- and pSTAT3-expressing elements characterized by pro-inflammatory and immunosuppressive features in COVID-19.

vFLIP overexpression in myeloid cell lineage induced pulmonary and systemic pathological features of CRS, including the fatal outcome

Since transgenic mice expressing v-FLIP in myeloid cells die prematurely within 4 weeks of life due to systemic immune disorders [35], we engrafted sub-lethally ablated, immunocompetent mouse recipients with bone marrow (BM) isolated from either ROSA26.vFLIP;LyzM-CRE (CD45.2) or wild type mice (CD45.1) mixed together at different ratios. All engrafted mice developed weight loss (Supplementary information, Fig. S2A-B), systemic

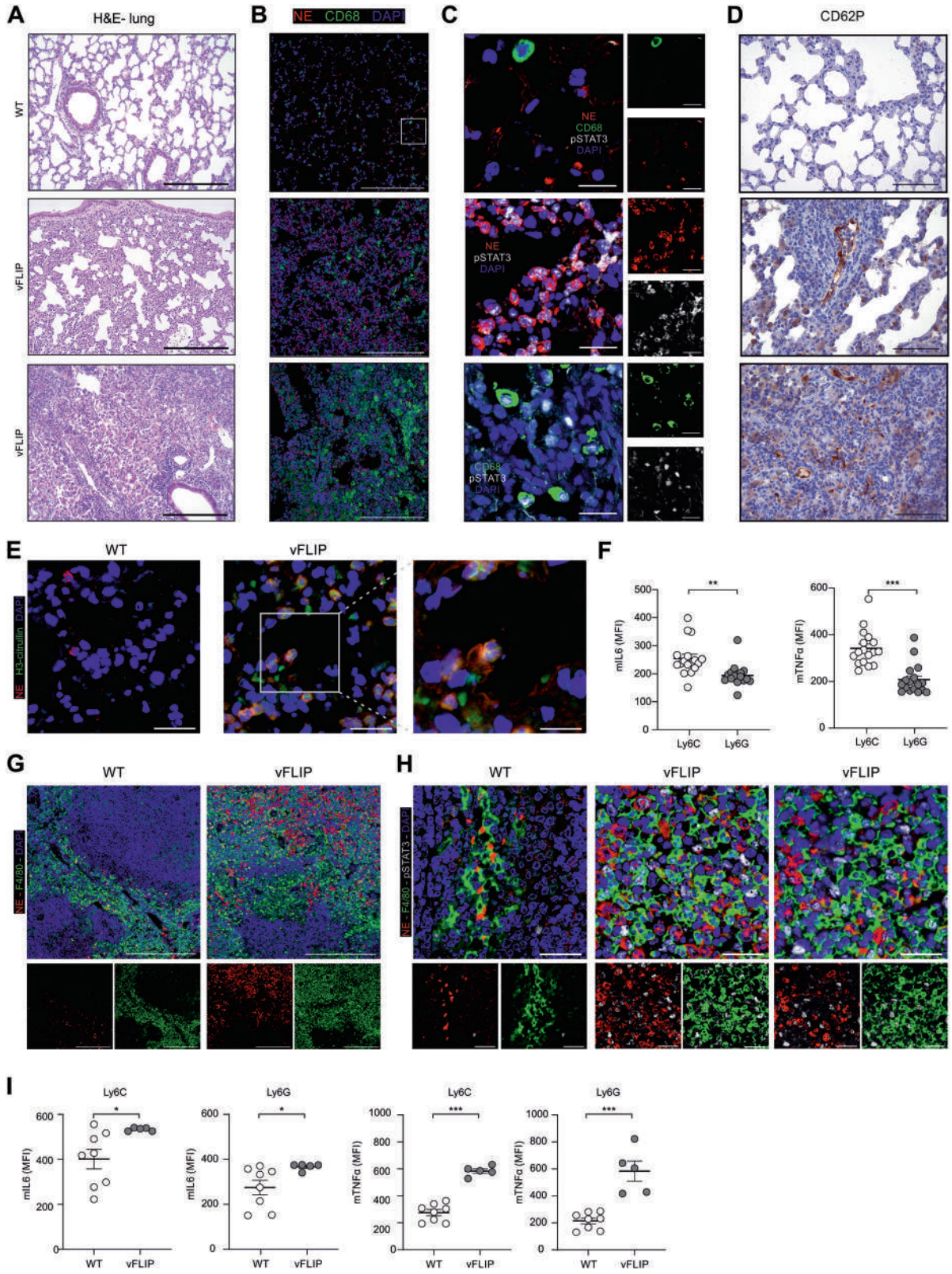

lymphopenia, and extensive accumulation of myeloid cells in the spleen, where a subversion of splenic architecture was marked (Supplementary information, Fig. S2C), as well as in several organs leading to the development of multi-organ injuries and areas of fibrosis (Supplementary information, Fig. S2D), including the lung. For subsequent analyses in this study, we employed BM chimeras (hereafter defined vFLIP mice), generated by transplantation of a 1:1 ratio of vFLIP^{+} and WT BM cells.

Since lung inflammation is the principal cause of life-threatening respiratory syndrome in CRS, including severe forms

Fig. 2 Local and systemic pSTAT3-dependent inflammation in vFLIP mice. A Representative H&E-stained microscopy images of lung of WT (upper panel) or vFLIP chimera mice. Scale bar, 200 μm. **B** Representative IF staining of lung-infiltrating neutrophils (NE^+ cells) and mononuclear phagocytes ($CD68^+$ cells) in WT or vFLIP mice. Cells were stained for DAPI (blue), neutrophil elastase (NE) (red, middle panel), and CD68 (green, bottom panel). Scale bar, 200 μm. **C** Representative IF staining of lung-infiltrating neutrophils and mononuclear phagocytes in WT or vFLIP mice. Scale bar, 20 μm. Cells were stained for DAPI (blue), NE (red, middle panel) or CD68 (green, bottom panel), and pSTAT3 Tyr705 (gray). **D** P-selectin (CD62P) presence in lung of WT (upper panel) or vFLIP mice by H&E staining. Scale bar, 100 μm. **E** Representative confocal analysis of NET in the lung of WT (left panel; 50 μm) or vFLIP mice (200 μm). Cells were stained for DAPI (blue), NE (red), and H3cit (green). **F** Dot plots of IL-6 and TNF-α in lung-infiltrating mononuclear phagocytes ($CD45.2^+Ly6C^+$ cells) and neutrophils ($CD45.2^+Ly6G^+$ cells) isolated from vFLIP mice ($n = 17$). **G** Representative IF staining of spleen-infiltrating neutrophils (NE^+ cells) and mononuclear phagocytes ($F4/80^+$ cells) in WT or vFLIP mice. Cells were stained for DAPI (blue), NE (red, middle panel), and F4/80 (green, bottom panel). Scale bar, 200 μm. **H** Representative IF staining of spleen-infiltrating neutrophils and mononuclear phagocytes in WT or vFLIP mice. Cells were stained for DAPI (blue), NE (red, middle panel), or F4/80 (green, bottom panel), and pSTAT3 Tyr705 (gray). **I** Dot plots of IL-6 and TNF-α in mononuclear ($Ly6C^+$ cells) and polymorphonuclear ($Ly6G^+$ cells) myeloid cells in spleen of WT ($n = 8$) or vFLIP mice ($n = 9$). Data are reported as mean ± S.E.M. $*p \le 0.05$, $**p \le 0.01$, and $***p \le 0.001$ by Mann–Whitney test.

of COVID-19 [20], we assessed the lung histopathology in vFLIP mice. Lungs of vFLIP mice showed diffuse interstitial myeloid infiltrate and alveolar damage, characterized by areas of fibrosis, lung consolidation, multinucleated cell clusters and tissue regions with peribronchial and perivascular infiltrate with associated intravascular thrombi. Severe cases also showed infarctions and extensive fibrosis (Fig. 2A, B, Supplementary information, Fig. S3A-D). Consistent with COVID-19 CRS, we detected pSTAT3 in both mononuclear phagocytes (hereafter identified as either $CD68^+$, $F4/80^+$ or $Ly6C^+$ cells) and neutrophils (hereafter identified as either NE^+ cells or $Ly6G^+$ cells) localized in vFLIP lung tissues compared to normal mice (Fig. 2C, Supplementary information, Fig. S3C). Considering the role of an aberrant immune response in the pathogenesis of COVID-19 by promoting alveolar inflammation and hyper-coagulation state in lung vessels [26, 82], we evaluated the presence of the endothelial dysfunction marker p-selectin (CD62P) in the pulmonary environment of vFLIP mice. P-selectin is normally stored in Weibel-Palade bodies of endothelial cells. After tissue injury, it is exposed in the vascular lumen where it mediates the adhesion and activation of platelets and leukocytes [83]. In vFLIP mice, p-selectin was strongly expressed on the luminal surface of inflamed vessels of large and small caliber, whereas it was not detectable in the lungs of WT mice (Fig. 2D).

Among effector mechanisms of neutrophils during inflammatory processes, neutrophil-derived extracellular traps (NETs) have been linked with the pathology of lung damage in COVID-19 [82]. In line with this evidence, NETs, identified as extracellular DNA staining colocalizing with NE and citrullinated histone H3 (H3Cit) by confocal microscopy [84], were not found in lung of WT mice but present in parenchima and alveoli of v-FLIP mice (Fig. 2E). Since several stimuli trigger neutrophil activation and NETosis, including inflammatory cytokines and chemokines [85, 86], we evaluated whether myeloid cells could be a source of these soluble factors. By intracellular staining, we enumerated TNF-α- and IL-6-producing mononuclear phagocytes ($CD45.2^+Ly6C^+$ cells) and neutrophils ($CD45.2^+Ly6G^+$ cells) isolated from the lung of vFLIP mice. We could not isolate sufficient number of myeloid cells from WT mouse lungs. Inflammatory cytokine production was higher in monocytes than in neutrophils (Fig. 2F). Notably, a marked accumulation of myeloid cells was identified also in the spleen of vFLIP mice (Fig. 2G), in which high percentages of $pSTAT3^+$ and inflammatory cytokine-producing monocytes were detected (Fig. 2H, I). We speculated that these cells might establish an unfavorable environment for T cells and, indeed, effector and helper T cells were heavily contracted while T regulatory lymphocytes (Tregs, identified as $CD4^+FoXP3^+$ cells) significantly expanded in the spleen of vFLIP mice (Supplementary information, Fig. S3E-F), unveiling a pronounced systemic lymphopenia that mirrors COVID-19-associated CRS.

To gain a broad insight into the immune landscape of CRS in vFLIP mice, we performed a single-cell RNA sequencing (scRNA-seq) on lung-infiltrating cells. After preprocessing, integration, and cell annotation (see the "Materials/subjects and methods" section), a total of 31,274 mouse cell transcriptomes were obtained across WT and vFLIP mice. All the cells were visualized through t-distributed stochastic neighbor embedding (t-SNE) assessing the cell proportions across the different mouse samples to have a global overview of the cell composition (Supplementary information, Fig. S4A-B). When we compared the percentage of each cell type across WT and vFLIP conditions (Fig. 3A), vFLIP mice showed a higher proportion of neutrophils (~65%) compared to WT mice (~23%) and a marked decrease in T (~5% vFLIP; ~17% WT) and B lymphocytes (~3% vFLIP; ~21% WT), confirming the aforementioned histopatological data about pulmonary infiltration of neutrophils (Fig. 2C). Conversely, monocytes (~9% vFLIP; ~12% WT) and macrophages (~13% vFLIP; ~16% WT) were comparable between the two groups.

To picture a global overview about biological pathways activated in vFLIP mice, we performed gene set enrichment analysis (GSEA) comparing vFLIP and WT cells. We noticed a significant upregulation in inflammatory responses, TNF-α signaling via NF-κB and JAK-STAT3 signaling pathway that were among the top enriched gene sets (Fig. 3B). Notably, these processes were related to the overexpression of several pro-inflammatory mediators such as Il1b, Ccrl2, Il1a, and Tnf (Fig. 3C). All these data are in line with results about pSTAT3 overexpression and TNF-α hyper-production in vFLIP mice (Fig. 2F), as well as previous data about FLIP controlling NF-κB [35, 87]. To link our results from vFLIP mice with Sars-Cov-2 infection, we matched GSEA results obtained from vFLIP mice with GSEA analysis of bulk RNA-Seq data of lung from hACE2 transgenic mouse infected with Sars-Cov-2 [88]. Comparing vFLIP upregulated pathways with those enriched following infection of hACE2 mice (day 7 post infection *vs* day 0, Fig. 3D), we found that SARS-CoV-2-induced inflammatory pathways were shared with vFLIP mice. Interestingly, these data are in line with transcriptomic analysis using additional animal models of SARS-CoV-2 infection [89]. Together, these results support the concept that CRS syndrome in vFLIP mouse model may mimic COVID-19 immunopathology.

vFLIP mice and COVID-19 patients display similar inflammatory myeloid cell landscapes in pulmonary environment

To compare the pulmonary immune landscape of vFLIP mice and COVID-19 patients, we quantified the similarity between mouse lung-infiltrating leukocytes and 19,996 immune cells isolated from bronchoalveolar lavage fluids (BAL) of severe COVID-19 patients ($n = 7$; WHO ordinal score 7) who were admitted to Intensive Care Units (ICU) of Verona Hospital [32]. A procedure similar to mouse cell integration and annotation was performed in order to assess cell composition in human BAL samples (Supplementary information, Fig. S4c-D). In both mouse and human datasets, neutrophils and monocyte/macrophage populations were separated and

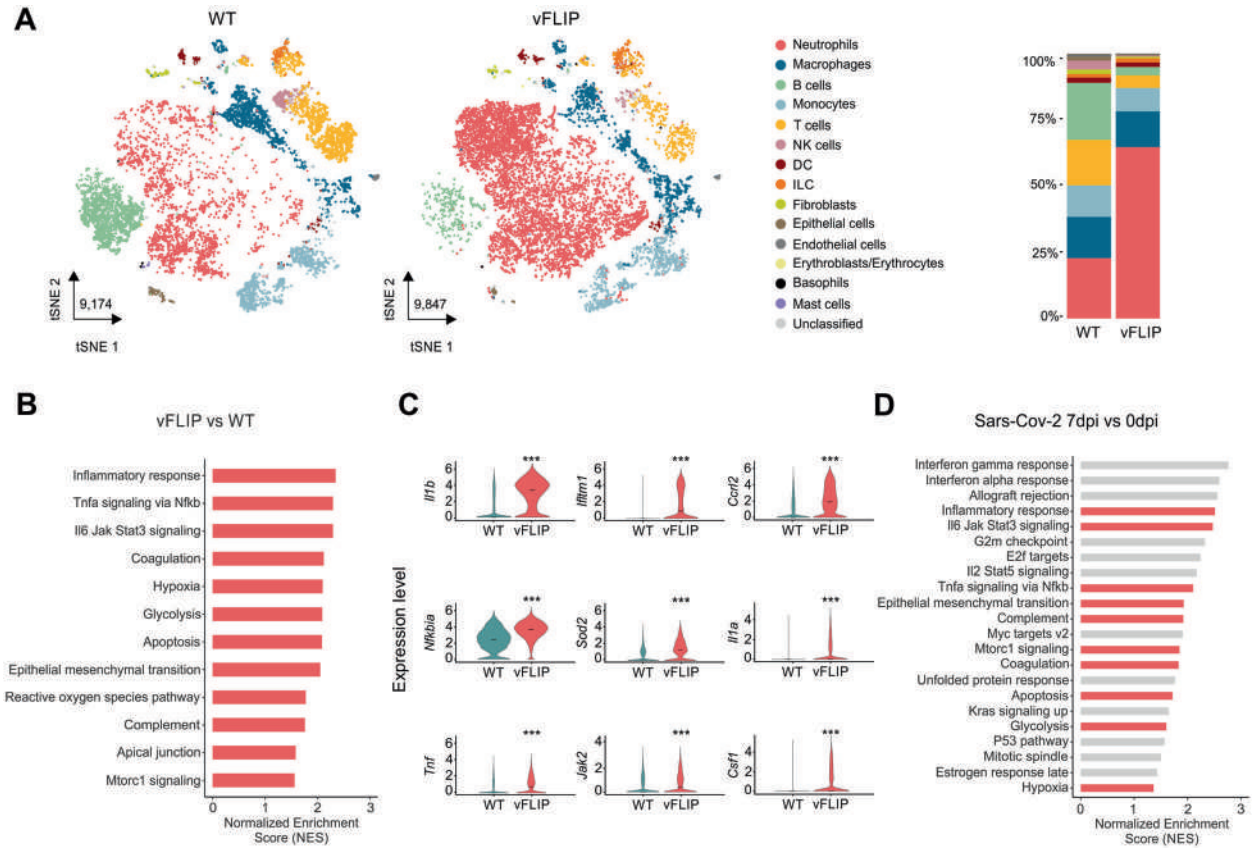

Fig. 3 Lung immune landscape in vFLIP mice affected by cytokine release syndrome. A tSNE representation of scRNA-seq from 2 WT and 2 vFLIP mice samples (WT: 9174; vFLIP: 9847) colored according to cell type. Stacked bar plots representing cell-type proportions across WT and vFLIP conditions. **B** Bar plot representing the upregulated (NES > 0, adjusted *p*-value <0.05) hallmark gene sets in the analysis of vFLIP vs WT cells obtained through GSEA analysis. **C** Violin plots showing the expression of key genes that drive the upregulation of inflammatory response, TNF-α signaling via NF-κB and JAK-STAT3 signaling pathway in the lung of vFLIP mice. The asterisks denote statistically significant upregulation in the comparison between vFLIP and WT conditions (*$p < 0.05$, **$p < 0.01$, ***$p < 0.001$). **D** Bar plot representing the upregulated (NES > 0, adjusted *p*-value <0.05) hallmark gene sets in bulk RNA-seq data obtained through GSEA analysis of ACE2-transgenic mice infected with Sars-CoV-2 [88] comparing day 7 post infection (dpi) with mock-infected (0 dpi). Red bars refer to the gene sets enriched in both vFLIP and ACE2-transgenic mice.

re-integrated prior to clustering, in order to have a better resolution in subset identification and comparison.

Following clustering, mouse neutrophils comprised 4 subsets characterized by canonical neutrophil markers including S100-family genes and *Adam8* (cluster 0), inflammatory chemokines *Ccl3* and *Ccl4* (cluster 1), high expression of *Camp* and *Ngp* genes (cluster 2), and interferon-response genes *Isg15/Isg20* (cluster 3) (Fig. 4A and Supplementary information, Dataset 1). Similarly, in COVID-19 BAL, we outlined 5 different clusters expressing marker genes similar to mouse neutrophil subsets. In particular, we observed clusters expressing canonical neutrophil markers such as *S100A8/S100A9* genes (cluster a), *CCL3/CCL4* chemokines as well as *CTSB* and *CSTB* genes (cluster b), interferon-response genes *IFIT1*, *IFIT2*, and *ISG15/ISG20* (cluster c) and other 2 clusters expressing ribosomal (cluster d) and heat shock protein (HSPs) genes (cluster e) (Fig. 4B and Supplementary information, Dataset 1).

We used reference-based classification (see the "Materials/subjects and methods" section) to map mouse subsets into human subsets. The results confirmed a conserved structure among neutrophil clusters between the two species and pathologies (Fig. 4C). In fact, about 89% of the human cluster c was annotated as cluster 3 of mouse, about 81% of cluster d was annotated as cluster 1 and, finally, clusters a, b, and e were mainly annotated as cluster 1 of mouse (60–65%). Conversely, cluster 2 appeared to be a mouse-specific neutrophil subset with no relevant correspondence in human subsets. These results recapitulate published reports [90], in which 3 conserved modules between mouse and human were characterized by the expression of *Ccl3/CCL3*, *Cstb/CSTB* (cluster 1 in vFLIP), type I interferon response genes such as *Ifit1/IFIT1*, *Irf7/IRF7*, and *Rsad2/RSAD2* (cluster 3 in vFLIP), and neutrophils expressing canonical markers *S100a8-a9/S100A8-A9* (cluster 0 in vFLIP).

Even though mouse clusters 1 and 3 were not the most abundant neutrophil subsets (Fig. 4A) in vFLIP mice, they were the most dysregulated in terms of cell proportion compared to WT. Indeed, Cluster 1 displayed more than twofold increase (~27% vFLIP; ~11% WT) while cluster 3 about threefold decrease in vFLIP compared to WT (~3% vFLIP; ~1% WT). Furthermore, GSEA analysis at the cluster level revealed several leading genes involved in neutrophil inflammatory response in cluster 1 (Supplementary information, Dataset 1), such as *Il1b*, *Ifitm1*, *Clec5A*, and *Ccrl2*, which were upregulated in vFLIP compared to WT mice (Fig. 4D and Supplementary information, Dataset 1).

We detected 7 clusters in mouse mononuclear phagocyte compartment (monocytes/macrophages) (Fig. 4E). Among macrophages, we could identify alveolar macrophages expressing *Mrc1*, *Krt79*, and *Krt19* genes (cluster 0), macrophages expressing either inflammatory cytokines such as *Cxcl3*, *Cxcl1*, and *Il1a* (cluster 4) or proliferation markers *Mki67* and *Top2a* (cluster 5), and a cluster expressing high levels of ribosomal genes (Cluster 6). In addition, we obtained a cluster composed by both macrophages (~64%) and monocytes (~36%) characterized by the expression of *C1qa* and

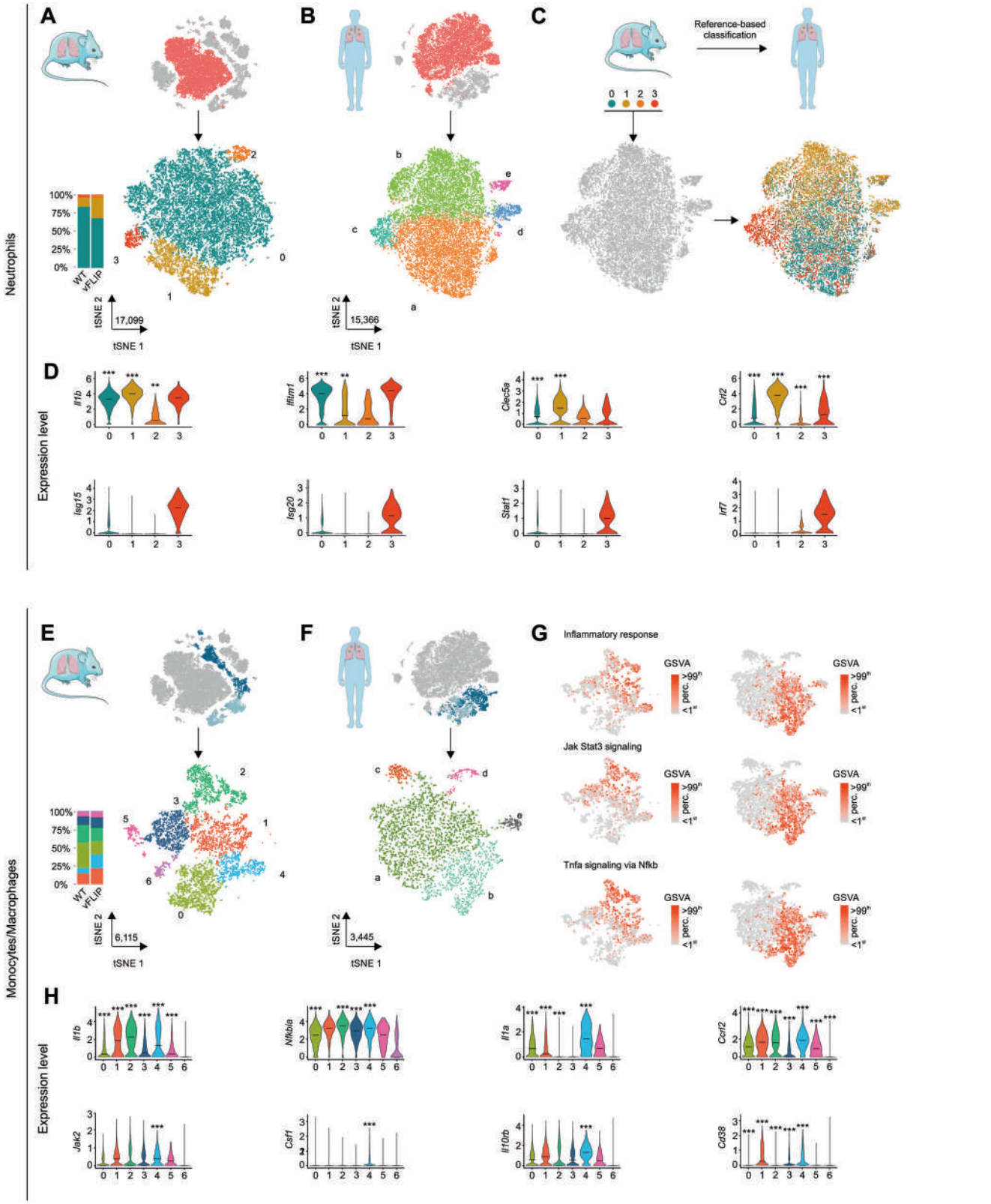

C1qb (cluster 1). Finally, among monocytes we detected classical monocytes expressing *Ccr2* and *Ly6c2* (cluster 3) and non-classical monocytes expressing *Ly6c2*, *Ace,* and *Cd300e* (cluster 2), reproducing the immune landscape previously described in tumor-bearing mice [90]. In monocytes/macrophages compartment from BAL patients, we observed 5 clusters (Fig. 4F): a macrophage cluster expressing proliferation markers *MKI67* and *TOP2A* (cluster d); a cluster characterized mainly by macrophages expressing *C1QA*, *C1QB*, and *MRC1* (cluster a); a cluster expressing monocyte markers *FCN1* and *VCAN* (cluster b); two small clusters expressing ribosomial

Fig. 4 Unbiased comparison between lung-infiltrating cells of vFLIP mice and BAL-derived immune cells obtained from COVID-19 patients. A tSNE representation and stacked bar plot showing cluster analysis of neutrophils coming from scRNA-seq analysis of lung tissue of mice ($n = 7$) and **B** COVID-19 patients BALs ($n = 7$). Neutrophils of mouse (17,099) and human (15,366) are visualized through tSNE projection and colored according to cluster analysis. **C** Reference-based classification of BAL neutrophil clusters using average expression of mice neutrophil clusters (see "Materials/subjects and methods"). **D** Violin plots showing the expression of key inflammatory and interferon response genes among mouse neutrophil clusters. The asterisks denote statistically significant upregulation in the comparison between vFLIP and WT conditions (*$p < 0.05$, **$p < 0.01$, ***$p < 0.001$). **E** Subset analysis of monocytes/macrophages of mouse ($n = 7$) and **F** COVID-19 BALs ($n = 7$). Monocytes/macrophages of mouse (6115) and human (3445) are visualized through tSNE projection and colored according to cluster analysis. **G** GSVA scores for inflammatory response, JAK-STAT3 signaling, and TNF-α signaling via NF-κB pathway across mouse (left) and BAL (right) monocytes/macrophage clusters. **H** Violin plots showing the expression level of key inflammatory response and JAK-STAT3 signaling pathway genes across mouse monocytes/macrophages subsets. The asterisks denote statistically significant upregulation in the comparison between vFLIP and WT conditions (*$p < 0.05$, **$p < 0.01$, ***$p < 0.001$).

(cluster c) and heat shock protein (HSPs) genes (cluster e). Probably due to the intrinsic complexity [90] and the low number of cells in the mononuclear phagocyte compartment [32], we were not able to distinguish classical from non-classical monocytes as well as to identify different macrophage subsets in BAL samples. Despite these caveats, we observed the expression of similar top marker genes between subset 5 and d, which identified proliferating macrophages (Supplementary information, Dataset 1); furthermore, the expression of several macrophage lineage genes such *C1QA*, *C1QB*, and *MRC1* was shared between the two species. Conversely, inflammatory genes such as *IL1B*, *CXCL1*, and *CXCL3* were mainly expressed by monocytes in BALs, unlike mouse dataset in which they were expressed at high levels both in monocyte and macrophages (Supplementary information, Dataset 1). Through gene set variation analysis (GSVA), we confirmed that inflammatory response and related pathways TNF-α signaling via NF-κB and JAK-STAT3 signaling were active in several clusters of mouse monocytes and macrophages while in BALs were specifically localized in monocytes (Fig. 4G). Despite several mouse subsets presented an upregulation of inflammatory genes in vFLIP compared to WT mice (Fig. 4H, top panels) as well as high GSVA scores on inflammatory-related pathways (Fig. 4G), GSEA analysis at the cluster level unveiled significant upregulation of inflammatory response, TNF-α signaling via NF-κB and JAK-STAT3 pathways specifically in cluster 4 (Supplementary information, Dataset 1), which was also the most dysregulated in terms of cell proportion (~19% vFLIP; ~8% WT) (Fig. 4E). Notably, the upregulation of JAK-STAT3 signaling pathway, in vFLIP cluster 4 compared to WT, was paralleled by the expression of several genes in the pathway such as *Jak2*, *Csf1*, *Il10rb*, and *Cd38* (Fig. 4H, bottom panels).

In summary, a conserved landscape of myeloid cells enriched for transcriptional signatures associated with the inflammatory response was detailed in the lung environment of both vFLIP mice and severe COVID-19 patients, in line with the concept that FLIP-expressing myeloid cells drive lung pathology.

STAT3 targeting restrains immunopathology in vFLIP mice

To investigate whether targeting STAT3 could be sufficient to dampen the uncontrolled immune dysregulation in vFLIP mice, we evaluated therapeutic approaches involving either pharmacological or RNA interference of STAT3. Initially, we tested in vivo the efficacy of two STAT3 inhibitors: silibinin, a STAT3 inhibitor that blocks the Y705 phosphorylation-related and STAT3 dimerization [91], or baricitinib, a clinically-approved inhibitor of JAK1 and JAK2 able to interfere with STAT3 signaling activation [92]. Four weeks after the establishment of BM chimerism in recipients (T0), mice were treated every 2 days by intraperitoneal injection. Weight loss was significantly decreased in mice that had received the drug treatments (Supplementary information, Fig. S5A). Furthermore, STAT3 targeting reduced the plasma concentration of several pro-inflammatory cytokines (Fig. 5A), which are produced at abnormal levels in untreated vFLIP mice and are also a feature of COVID-19 [3]. Immunohistochemistry of spleen demonstrated a reduction in systemic lymphopenia of treated vFLIP mice, with some differences, since baricitinib furthered a raise in both T and B cells while silibinin affected only T lymphocyte frequency (Fig. 5B). By analyzing eight different parameters (e.g., interstitial enlargement, vascular congestion, perivascular neutrophils, presence of thrombi, presence of infarction, fibroplasia, foam cell clusters, and perivascular infiltrate; Supplementary information, Fig. S5B), we confirmed a reduction in the pathological score of inflammatory pneumonia in treated mice (Fig. 5C and Supplementary information, Fig. S5C).

To explore further the molecular underpinnings of the inflammatory shutdown, we evaluated the lung-infiltrating leukocyte profile of treated and untreated vFLIP mice by scRNA-seq. After projecting the cells into a two-dimensional space using t-SNE, we evaluated the effect of pharmacological treatments on the proportions of the main cellular subsets. Both treatments reduced the neutrophil proportion (~82% UT; ~76% silibinin; ~66% baricitinib), with a compensatory increase in other cells, such as lymphocytes, indicating a trend towards rebalancing the lung-infiltrating leukocyte frequency (Fig. 5D). Considering neutrophil subgroups, we observed a slight reduction in the major neutrophil subset (cluster 0: ~89% UT; ~87% silibinin; ~86% baricitinib) in treated mice and an expansion in neutrophils expressing interferon-response genes (cluster 3: ~2% UT; ~4% silibinin: ~5% baricitinib) (Supplementary information, Fig. S5D). Therefore, STAT3-targeting approaches can alter neutrophil composition favoring the accrual of elements with type I interferon response-associated genes. As for the monocytes/macrophages in treated mice, we observed a decrease in both classical monocytes (clusters 3: ~32% UT; ~23% silibinin; ~25% baricitinib) and macrophages expressing inflammatory cytokines (cluster 4: ~12% UT; ~8% silibinin; ~8% baricitinib); at the same time, we evinced the increase in clusters 1 (~25% UT; ~27% silibinin; ~41% baricitinib) and cluster 2 (non-classical monocytes: ~10% UT; ~20% silibinin; ~14% baricitinib) (Supplementary information, Fig. S5D).

Finally, GSEA analysis confirmed an upregulation of interferon alpha/gamma pathways in both STAT3-based treatments compared to controls and, simultaneously, the downregulation of gene signatures associated to inflammatory response, JAK-STAT3-dependent signaling pathways, and TNF-α signaling via NF-κB (Fig. 5E). Consistent with this effect, several inflammatory genes, such as *Il1b, Clec5a, Ccrl2*, and *Ifitm1* were downregulated while *Ifitm3*, *Stat1*, and *Isg15* genes, which are associated to interferon response pathways, were upregulated in baricitinib-treated vFLIP mice (Fig. 5F). Thus, STAT3 inhibitors might mitigate the inflammatory pathology, both locally and systemically, by affecting the aberrant FLIPs-STAT3 feedforward loop while keeping the antiviral response active.

To confirm the immunomodulatory capacity of STAT3 inhibitors, we tested the ability of these two compounds to control the immunosuppressive functions of c-FLIP-expressing monocytes isolated from COVID-19 patients. T-cell proliferation was significantly preserved after co-culture with monocytes pre-treated with the two drugs, as compared to untreated controls (Supplementary

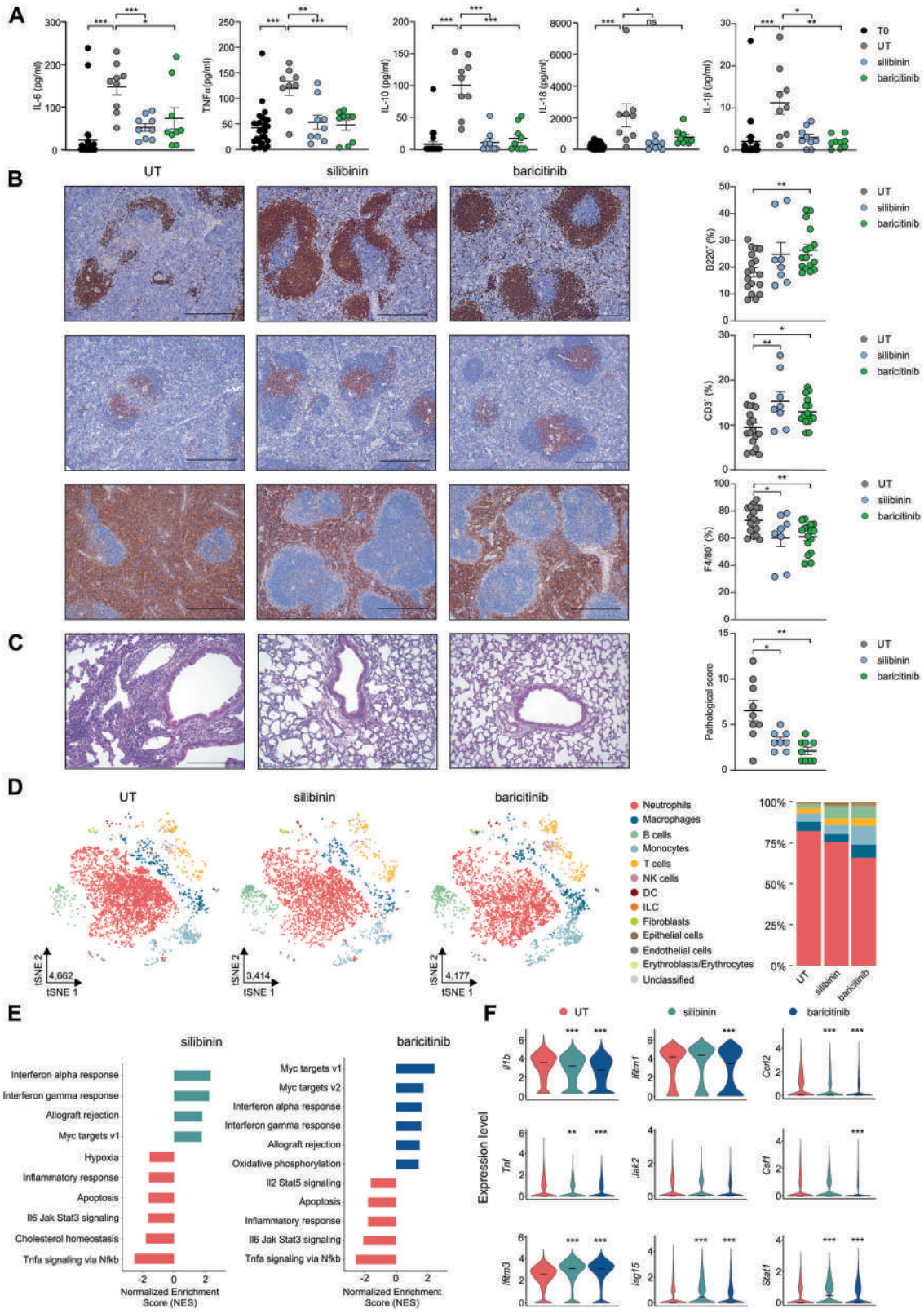

information, Fig. S5E). These results indicate that STAT3-targeting may prevent T-cell dysregulations by limiting immunosuppressive features of SARS-CoV-2-educated myeloid cells, endorsing the clinical results about baricitinib efficacy in altering immunoregulatory properties of myeloid cells in COVID-19 patients [80].

To provide complementary evidence that a direct STAT3-silencing in myeloid cells could control the evolution of immunopathological disorders in vFLIP mice, we exploited the in vivo delivery of 4PD nanoparticles loaded with STAT3-specific short hairpin RNAs (shSTAT3) on their surface. The ability of 4PDs

Fig. 5 STAT3 pharmacological targeting reduces lung damage and immune dysfunctions in vFLIP mice. A Analysis of cytokines levels in serum of vFLIP mice before treatment (T0) or at the end of treatment (untreated, $n = 9$; silibinin, $n = 9$; baricitinib, $n = 9$). **B** Lymphocytes (B cells: $B220^+$ cells; T cells: $CD3^+$ cells) and macrophages ($F4/80^+$ cells) quantification in spleens of untreated ($n = 14$), silibinin ($n = 8$), and baricitinib ($n = 16$) vFLIP mice by H&E staining. Scale bar, 200 μm. **C** Pathological score of lungs of untreated ($n = 14$), silibinin ($n = 8$), and baricitinib ($n = 16$) vFLIP mice by H&E staining. Scale bar, 200 μm. **D** tSNE representation of scRNA-seq from untreated (4662) mice and treated with silibinin (3414) and baricitinib (4177) colored according to cell type. Stacked bar plots representing cell-type proportions across conditions. **E** Bar plot representing the up- and downregulated (adjusted *p*-value <0.05) hallmark gene sets obtained in the bulk-like analysis of treated compared to untreated vFLIP chimera cells obtained through GSEA analysis. **F** Violin plots showing the expression of genes involved in inflammatory response, JAK-STAT3 signaling pathway, and interferon response in the lung of vFLIP chimera mice (*$p < 0.05$, **$p < 0.01$, ***$p < 0.001$). Data are reported as mean ± S.E.M. *$p \le 0.05$, **$p \le 0.01$, and ***$p \le 0.001$ by Student's *t*-test, Mann–Whitney test.

to recognize and target preferentially mononuclear phagocytes and mediate an effective in vivo delivery of shSTAT3 was previously proven in cancer mouse models [45]. Therefore, vFLIP mice were treated by a total of nine administrations, every 2 days, of 4PDs loaded with either a scrambled RNA sequence (shCTRL, as negative control) or shSTAT3. Similar to STAT3 pharmacological treatment, the genetically-based STAT3 silencing in myeloid compartment controlled the weight loss, limiting CRS-associated cachexia (Supplementary information, Fig. S6A). Moreover, STAT3-silencing affected the severity of inflammatory pneumonia, as highlighted by the decrease in lung pathological score (Fig. 6A and Supplementary information, Fig. S6B) and allowed a strong contraction of in both neutrophilia and inflammation within pulmonary tissues (Fig. 6B and Supplementary information, Fig. S6C). Notably, shSTAT3 treated mice showed also a reduction in systemic lymphopenia, with an increased frequency of both T and B lymphocytes and a concomitant myeloid cell reduction in the spleen (Fig. 6C) and in peripheral blood (Fig. 6D). Finally, the 4PD-mediated, STAT3-specific shRNA delivery normalized the plasma concentration of several pro-inflammatory cytokines (Fig. 6E). Taken together, these data indicate that STAT3-targeting, especially in myeloid cells, is effective in tempering CRS-associated immunopathological disorders triggered by the accumulation of FLIP-expressing cells.

DISCUSSION

To date, the pathology of CRS is incompletely understood and no single definition is widely accepted by the scientific community. Our data establish FLIP-expressing myeloid cells as a pivotal driver of CRS. Indeed, the vFLIP chimera mice show acute systemic inflammatory symptoms (Fig. 2 and Supplementary information, Figs. S2–3), elevated cytokine levels (Fig. 5A), weight loss (Supplementary information, Fig. S5A), lymphopenia (Supplementary information, Fig. S2C), lung injury (Fig. 2A) endothelial cell activation (Fig. 2D) and multiple organ dysfunctions (Supplementary information, Fig. S2D). The impact of vFLIP activation on building up inflammatory diseases is confirmed also by evidence about the role of this anti-apoptotic protein in inflammatory bowel disease [93], multicentric Castleman disease in mice [94], as well as on reprogramming myeloid cells into immunosuppressive elements in cancer [35].

A significant gap remains between pre-clinical testing and clinical trials to treat efficiently CRS, as well as to identify key molecular mechanisms that control the pathogenic process. In the last decades, mouse models of sepsis, such as LPS-induced inflammation, or the development of humanized mice based on the engraftment of human PBMCs into immunodeficient mice, which mimic CAR T-cell therapy-induced cytokine storm, have been primarily developed to replicate clinical stages and outcomes of CRS, as platforms for screening potential therapies [6, 95]. However, no suitable and appropriate experimental in vivo models have been developed to identify alterations in molecular and cellular processes that might highlight the triggers of CRS. Our study based on a tissue-specific transgenic, conditional knock-in mouse model offer a novel tool for defining the mechanisms that fuel inflammation and CRS-associated immune dysfunctions.

In line with our results, recent studies underlined that c-FLIP expression was enhanced in several SARS-CoV-2-infected cell lines, where the expression of FLIP suppressors, such as the forkhead transcriptional factor FoxO3A [96], was abrogated [30, 97]. Since the interaction of c-FLIP to FADD and/or caspase-8 or -10 and TRAIL receptor 5 prevents death-inducing signaling complex formation and subsequent activation of the caspase cascade [98], it is plausible that SARS-CoV-2 virus exploits FLIP-mediated cell death delay for its own replication. Our analysis of both SARS-CoV-2-infected hACE2 transgenic mice and autopsy samples from lung in COVID-19 patients demonstrated, for the first time, the in vivo overexpression of FLIP in myeloid cells in severe COVID-19 (Fig. 1). However, compared to the traditionally ascribed FLIP intervention on cell survival, our findings rather point to the additional function of modulating myeloid cells to determine CRS progression (Fig. 1D, E; Fig. 2I).

Monocytes from both COVID-19 patients (Fig. 1C) and vFLIP transgenic mice [35] display immunosuppressive properties and are a source of pro-inflammatory cytokines (Fig. 1E and Supplementary information, Fig. S1G). We found that immunoregulatory functions of monocytes isolated from COVID-19 patients correlated with the expression of PD-L1 (Supplementary information, Fig. S1F), suggesting a possible contribution of immune checkpoint engagement on T cell blockade during COVID-19 evolution. These data are in line with our previous findings showing that FLIP-expressing monocytes isolated from PDAC patients had high levels of surface PD-L1 [35] and confirm previous reports indicating that immunosuppressive myeloid cells in COVID-19 patients did exhibit increased *CD274* mRNA levels [32, 34]. In agreement with Schulte-Schrepping's report in which STAT3 was suspected as transcriptional factor of immunosuppressive monocytes in COVID-19, we demonstrated that immunosuppression by monocytes isolated from COVID-19 patients can be indeed reverted by STAT3 inhibitors (Supplementary information, Fig. S5E). Furthermore, we unveiled a concomitant expression of FLIP and activated STAT3 signaling in myeloid cells of SARS-CoV-2-infected hosts (Fig. 1A and F), as well as in vFLIP transgenic mouse model (Fig. 2C). Further investigations should mechanistically address the unconventional properties of c-FLIP as transcription factor, either by itself or cofactor of transcriptional machinery capable of activating STAT3 signaling pathway in myeloid cells under pathological conditions, which to date are only partially demonstrated in immortalized cell lines [43, 99].

Since the in vitro enforced expression of FLIP in myeloid cells promotes the overexpression of several pro-inflammatory cytokines (i.e., IL-6, IL-7, IL-10, CSF3, and TNF-α) by a "steered" NF-κB activation, which also results in enhanced STAT3-signaling activation [35], we argue that a pervasive inflammatory loop is established by FLIP through the joint action of NF-κB and STAT3 during CRS evolution. Indeed, a synergy between NF-κB and STAT3 molecules based on pro-inflammatory cytokines (i.e., IL-6), which act as inflammation amplifier, was reported in several multiple inflammatory and autoimmune diseases [100] and postulated also in COVID-19 [101]. In agreement with this

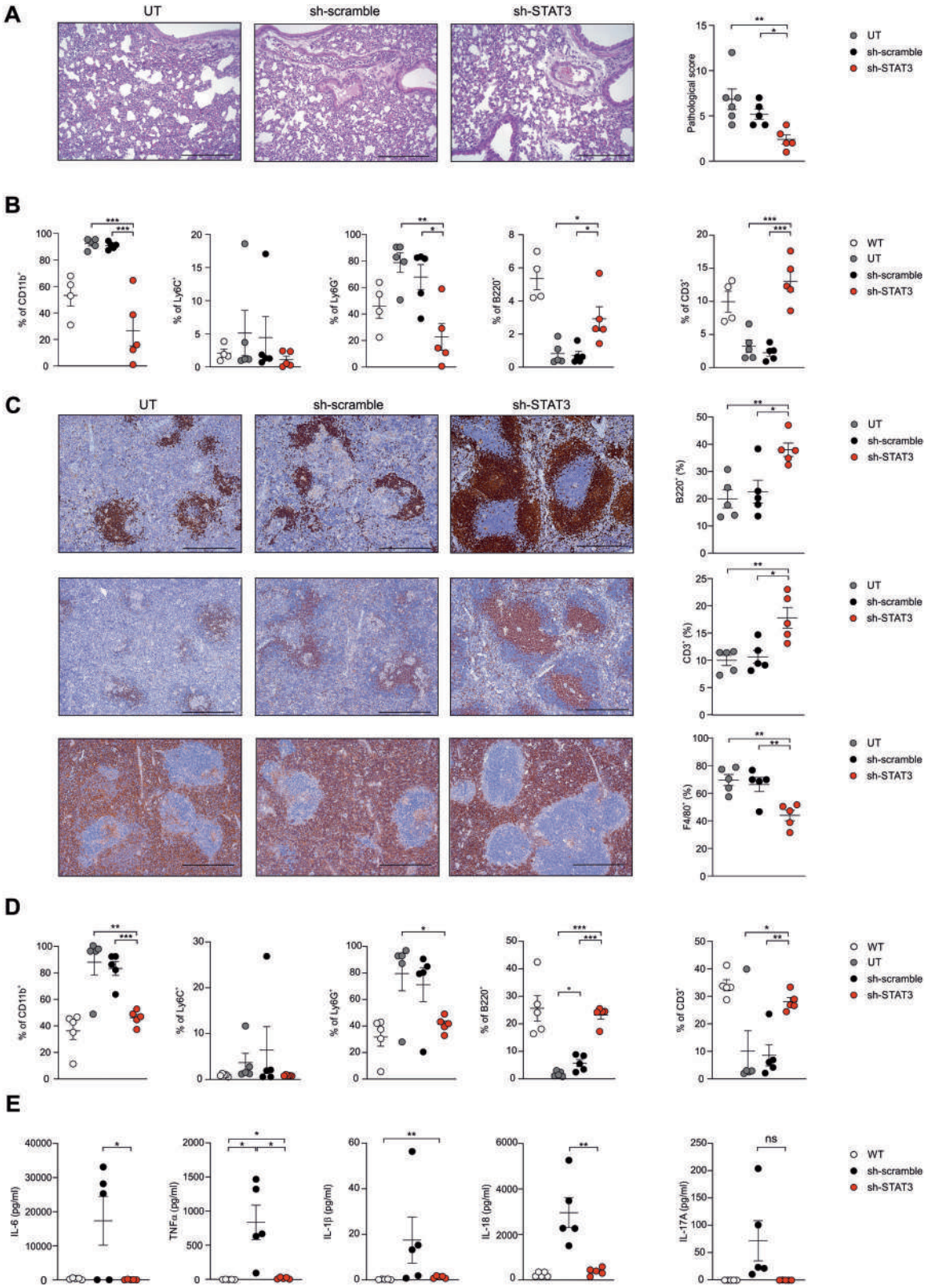

paradigm, a recent analysis of multi-organ proteomic landscape of COVID-19 autopsies confirmed both NF-κB and STAT3 as transcription factors largely upregulated in multiple organs [102], implying a widespread and pervasive activations of the two pathways. Conversely, we did not uncover a global alteration in type I IFN response in vFLIP mice compared to WT mice, suggesting that CRS progression in vFLIP mice is independent from IFN-I-associated pathway while IFN-I response during Coronavirus infection plays a critical role, at least in the initial phases of viral control. This discrepancy likely relies on the fact

Fig. 6 In vivo STAT3-silencing approach mitigates the evolution of immunopathological disorders in vFLIP mice. A Pathological score of lungs of vFLIP mice (untreated, $n = 6$; sh-scramble, $n = 5$; sh-STAT3, $n = 5$) by H&E staining. Scale bar, 200 μm. **B** Flow cytometry analysis of myeloid cells ($CD11b^+$ cells), mononuclear phagocytes ($Ly6C^+$ cells), neutrophils ($Ly6G^+$ cells), B ($B220^+$ cells), and T ($CD3^+$ cells) lymphocytes isolated from lungs of vFLIP mice (untreated, $n = 6$; sh-scramble, $n = 5$; sh-STAT3, $n = 5$) or WT mice ($n = 5$). **C** Lymphocytes (B cells: $B220^+$ cells; T cells: $CD3^+$ cells) and macrophages ($F4/80^+$ cells) quantification in spleens of vFLIP mice (untreated, $n = 6$; sh-scramble, $n = 5$; sh-STAT3, $n = 5$) by H&E staining. Scale bar, 400 μm. **D** Flow cytometry analysis in peripheral blood of myeloid cells ($CD11b^+$ cells), mononuclear phagocytes ($Ly6C^+$ cells), neutrophils ($Ly6G^+$ cells), B ($B220^+$ cells), and T ($CD3^+$ cells) lymphocytes in vFLIP mice (untreated, $n = 6$; sh-scramble, $n = 5$; sh-STAT3, $n = 5$) or WT mice ($n = 5$). **E** Analysis of cytokines levels in serum of WT ($n = 5$), sh-scramble ($n = 5$), or sh-STAT3 ($n = 5$) vFLIP mice. Data are reported as mean ± S.E.M. $*p \le 0.05$, $**p \le 0.01$, and $***p \le 0.001$ by Mann–Whitney test.

that vFLIP model mimics only the late phase of COVID-19-disease, which is characterized by exacerbated inflammation.

Our in vivo findings show that STAT3-targeting provides a significant disease control in mice with CRS, unexpectedly highlighting how blocking a single member of the NF-κB/STAT3 loop is sufficient to halt pathological inflammation. Data presented here are in line with recent clinical results about baricitinib efficacy in controlling SARS-CoV-2-mediated immune dysregulation [80, 89, 103, 104] and with the decision of U.S. Food and Drug Administration to approve baricitinib as monotherapy in hospitalized adults and pediatric patients 2 years of age or older [105], as well as in combination with remdesivir for the treatment of severe COVID-19 patients. More important, we demonstrated that Jak1/Jak2 inhibitor did not affect negatively genes associated with type I IFN antiviral responses but, on the contrary, pharmacological treatment was associated with a relative increase in interferon-stimulated genes (Fig. 5E, F), likely by reprogramming the myeloid composition in the lung environment (Fig. 5D and Supplementary information, Fig. S5C). This signaling switch might be due to the activity of STAT1 occupying space on STAT3-activating receptors, as suggested by the conversion of IL-6R signaling to a dominant STAT1 activation in STAT3-deficient cells [106, 107]. Finally, the striking results on the normalization of the immune landscape, organ pathology, and cachexia following shSTAT3-based treatment (Fig. 6 and Supplementary information, Fig. S6) clearly finger at STAT3 as the main target in FLIP-expressing myeloid cells and define it as the most deleterious cause of immune and tissue damage during CRS.

Despite the caveats linked to species-specific profiles, our findings revealed some conserved genetic features of lung-infiltrating myeloid cells between vFLIP mice and COVID-19 patients. Indeed, neutrophil subsets characterized by the expression of S100-family genes, type I interferon response genes (ISG15/ISG20), and chemokines (*Ccl3*/*CCL3*), as well as macrophages expressing proliferation-associated gene signatures (*Mki67*, *Top2a*) showed similarities among species. The shared leukocyte subsets showed a higher expression of inflammatory response-associated genes and were more prone to STAT3 therapy.

In summary, in this study, we demonstrated the pivotal role of FLIP-expressing myeloid cells to stimulate directly a lethal inflammatory status, by fueling an aberrant STAT3-dependent signaling pathway. Moreover, we substantiated the therapeutic effectiveness of STAT3 on-target strategy to mitigate uncontrolled inflammation and acute disease, which serve as a foundation for the development of more accurate and evidence-based therapies to control CRS disorders, as well as severe clinical aspects of the ongoing COVID-19 pandemic crisis.

DATA AVAILABILITY

The scRNA-seq data generated in this study have been deposited in the Gene Expression Omnibus (GEO) under accession number GSE168098. Human scRNA-seq data from bronchoalveolar lavage fluids (BALs) was obtained from GEO under accession GSE157344.

REFERENCES

1. Griffith JW, Sokol CL, Luster AD. Chemokines and chemokine receptors: positioning cells for host defense and immunity. Annu Rev Immunol. 2014;32:659–702.
2. Rieger MA, Hoppe PS, Smejkal BM, Eitelhuber AC, Schroeder T. Hematopoietic cytokines can instruct lineage choice. Science. 2009;325:217–8.
3. Fajgenbaum DC, June CH. Cytokine storm. N Engl J Med. 2020;383:2255–73.
4. de Jong MD, Simmons CP, Thanh TT, Hien VM, Smith GJ, Chau TN, et al. Fatal outcome of human influenza A (H5N1) is associated with high viral load and hypercytokinemia. Nat Med. 2006;12:1203–7.
5. van der Poll T, Opal SM. Host-pathogen interactions in sepsis. Lancet Infect Dis. 2008;8:32–43.
6. Norelli M, Camisa B, Barbiera G, Falcone L, Purevdorj A, Genua M, et al. Monocyte-derived IL-1 and IL-6 are differentially required for cytokine-release syndrome and neurotoxicity due to CAR T cells. Nat Med. 2018;24:739–48.
7. Giavridis T, van der Stegen SJC, Eyquem J, Hamieh M, Piersigilli A, Sadelain M. CAR T cell-induced cytokine release syndrome is mediated by macrophages and abated by IL-1 blockade. Nat Med. 2018;24:731–8.
8. Obstfeld AE, Frey NV, Mansfield K, Lacey SF, June CH, Porter DL, et al. Cytokine release syndrome associated with chimeric-antigen receptor T-cell therapy: clinicopathological insights. Blood. 2017;130:2569–72.
9. Winkler U, Jensen M, Manzke O, Schulz H, Diehl V, Engert A. Cytokine-release syndrome in patients with B-cell chronic lymphocytic leukemia and high lymphocyte counts after treatment with an anti-CD20 monoclonal antibody (rituximab, IDEC-C2B8). Blood. 1999;94:2217–24.
10. Teachey DT, Rheingold SR, Maude SL, Zugmaier G, Barrett DM, Seif AE, et al. Cytokine release syndrome after blinatumomab treatment related to abnormal macrophage activation and ameliorated with cytokine-directed therapy. Blood. 2013;121:5154–7.
11. Abboud R, Keller J, Slade M, DiPersio JF, Westervelt P, Rettig MP, et al. Severe cytokine-release syndrome after T cell-replete peripheral blood haploidentical donor transplantation is associated with poor survival and anti-IL-6 therapy is safe and well tolerated. Biol Blood Marrow Transpl. 2016;22:1851–60.
12. Fajgenbaum DC, Langan RA, Japp AS, Partridge HL, Pierson SK, Singh A, et al. Identifying and targeting pathogenic PI3K/AKT/mTOR signaling in IL-6-blockade-refractory idiopathic multicentric Castleman disease. J Clin Invest. 2019;129:4451–63.
13. Pierson SK, Stonestrom AJ, Shilling D, Ruth J, Nabel CS, Singh A, et al. Plasma proteomics identifies a 'chemokine storm' in idiopathic multicentric Castleman disease. Am J Hematol. 2018;93:902–12.
14. Matthay MA, Ware LB, Zimmerman GA. The acute respiratory distress syndrome. J Clin Invest. 2012;122:2731–40.
15. Huang C, Wang Y, Li X, Ren L, Zhao J, Hu Y, et al. Clinical features of patients infected with 2019 novel coronavirus in Wuhan, China. Lancet. 2020;395:497–506.
16. Studdert DM, Hall MA. Disease control, civil liberties, and mass testing—calibrating restrictions during the Covid-19 pandemic. N Engl J Med. 2020;383:102–4.
17. Wang C, Horby PW, Hayden FG, Gao GF. A novel coronavirus outbreak of global health concern. Lancet. 2020;395:470–3.
18. Zhou P, Yang XL, Wang XG, Hu B, Zhang L, Zhang W, et al. A pneumonia outbreak associated with a new coronavirus of probable bat origin. Nature. 2020;579:270–3.
19. Guan WJ, Ni ZY, Hu Y, Liang WH, Ou CQ, He JX, et al. Clinical characteristics of coronavirus disease 2019 in China. N Engl J Med. 2020;382:1708–20.
20. Xu Z, Shi L, Wang Y, Zhang J, Huang L, Zhang C, et al. Pathological findings of COVID-19 associated with acute respiratory distress syndrome. Lancet Respir Med. 2020;8:420–2.
21. Doglioni C, Ravaglia C, Chilosi M, Rossi G, Dubini A, Pedica F, et al. Covid-19 Interstitial Pneumonia: Histological and Immunohistochemical Features on Cryobiopsies. Respiration. 2021;100:488–98.

22. Carsana L, Sonzogni A, Nasr A, Rossi RS, Pellegrinelli A, Zerbi P, et al. Pulmonary post-mortem findings in a series of COVID-19 cases from northern Italy: a two-centre descriptive study. Lancet Infect Dis. 2020;20:1135–40.
23. McGonagle D, O'Donnell JS, Sharif K, Emery P, Bridgewood C. Immune mechanisms of pulmonary intravascular coagulopathy in COVID-19 pneumonia. Lancet Rheumatol. 2020;2:e437–45.
24. Gupta A, Madhavan MV, Sehgal K, Nair N, Mahajan S, Sehrawat TS, et al. Extrapulmonary manifestations of COVID-19. Nat Med. 2020;26:1017–32.
25. Varga Z, Flammer AJ, Steiger P, Haberecker M, Andermatt R, Zinkernagel AS, et al. Endothelial cell infection and endotheliitis in COVID-19. Lancet. 2020;395: 1417–8.
26. Ackermann M, Verleden SE, Kuehnel M, Haverich A, Welte T, Laenger F, et al. Pulmonary vascular endothelialitis, thrombosis, and angiogenesis in Covid-19. N Engl J Med. 2020;383:120–8.
27. Mehta P, McAuley DF, Brown M, Sanchez E, Tattersall RS, Manson JJ. COVID-19: consider cytokine storm syndromes and immunosuppression. Lancet. 2020;395: 1033–4.
28. Barnes BJ, Adrover JM, Baxter-Stoltzfus A, Borczuk A, Cools-Lartigue J, Crawford JM, et al. Targeting potential drivers of COVID-19: neutrophil extracellular traps. J Exp Med. 2020;217:1–7.
29. Carvelli J, Demaria O, Vély F, Batista L, Chouaki Benmansour N, Fares J, et al. Association of COVID-19 inflammation with activation of the C5a-C5aR1 axis. Nature. 2020;588:146–50.
30. Blanco-Melo D, Nilsson-Payant BE, Liu WC, Uhl S, Hoagland D, Møller R, et al. Imbalanced host response to SARS-CoV-2 drives development of COVID-19. Cell. 2020;181:1036–45.
31. Schultze JL, Aschenbrenner AC. COVID-19 and the human innate immune system. Cell. 2021;184:1671–92.
32. Bost P, De Sanctis F, Canè S, Ugel S, Donadello K, Castellucci M, et al. Deciphering the state of immune silence in fatal COVID-19 patients. Nat Commun. 2021;12:1428.
33. Del Valle DM, Kim-Schulze S, Huang HH, Beckmann ND, Nirenberg S, Wang B, et al. An inflammatory cytokine signature predicts COVID-19 severity and survival. Nat Med. 2020;26:1636–43.
34. Schulte-Schrepping J, Reusch N, Paclik D, Baßler K, Schlickeiser S, Zhang B, et al. Severe COVID-19 is marked by a dysregulated myeloid. Cell Compartment Cell. 2020;182:1419–40. e1423
35. Fiore A, Ugel S, De Sanctis F, Sandri S, Fracasso G, Trovato R, et al. Induction of immunosuppressive functions and NF-κB by FLIP in monocytes. Nat Commun. 2018;9:5193.
36. Thome M, Schneider P, Hofmann K, Fickenscher H, Meinl E, Neipel F, et al. Viral FLICE-inhibitory proteins (FLIPs) prevent apoptosis induced by death receptors. Nature. 1997;386:517–21.
37. Irmler M, Thome M, Hahne M, Schneider P, Hofmann K, Steiner V, et al. Inhibition of death receptor signals by cellular FLIP. Nature. 1997;388:190–5.
38. Sadek J, Wuo MG, Rooklin D, Hauenstein A, Hong SH, Gautam A, et al. Modulation of virus-induced NF-κB signaling by NEMO coiled coil mimics. Nat Commun. 2020;11:1786.
39. Golks A, Brenner D, Krammer PH, Lavrik IN. The c-FLIP-NH2 terminus (p22-FLIP) induces NF-kappaB activation. J Exp Med. 2006;203:1295–305.
40. Safa AR. c-FLIP, a master anti-apoptotic regulator. Exp Oncol. 2012;34:176–84.
41. Shisler JL. Viral and cellular FLICE-inhibitory proteins: a comparison of their roles in regulating intrinsic immune responses. J Virol. 2014;88:6539–41.
42. Katayama R, Ishioka T, Takada S, Takada R, Fujita N, Tsuruo T, et al. Modulation of Wnt signaling by the nuclear localization of cellular FLIP-L. J Cell Sci. 2010; 123:23–8.
43. Zhang J, Chen Y, Huang Q, Cheng W, Kang Y, Shu L, et al. Nuclear localization of c-FLIP-L and its regulation of AP-1 activity. Int J Biochem Cell Biol. 2009;41: 1678–84.
44. Cooke KR, Kobzik L, Martin TR, Brewer J, Delmonte J Jr, Crawford JM, et al. An experimental model of idiopathic pneumonia syndrome after bone marrow transplantation: I. The roles of minor H antigens and endotoxin. Blood. 1996;88: 3230–9.
45. Zilio S, Vella JL, De la Fuente AC, Daftarian PM, Weed DT, Kaifer A, et al. 4PD functionalized dendrimers: a flexible tool for in vivo gene silencing of tumor-educated myeloid cells. J Immunol. 2017;198:4166–77.
46. Butler A, Hoffman P, Smibert P, Papalexi E, Satija R. Integrating single-cell transcriptomic data across different conditions, technologies, and species. Nat Biotechnol. 2018;36:411–20.
47. Hafemeister C, Satija R. Normalization and variance stabilization of single-cell RNA-seq data using regularized negative binomial regression. Genome Biol. 2019;20:296.
48. Stuart T, Butler A, Hoffman P, Hafemeister C, Papalexi E, Mauck WM 3rd, et al. Comprehensive integration of single-cell data. Cell. 2019;177:1888–902.e1821.
49. Wolock SL, Lopez R, Klein AM. Scrublet: computational identification of cell doublets in single-cell transcriptomic data. Cell Syst. 2019;8:281–91.e289.
50. Aran D, Looney AP, Liu L, Wu E, Fong V, Hsu A, et al. Reference-based analysis of lung single-cell sequencing reveals a transitional profibrotic macrophage. Nat Immunol. 2019;20:163–72.
51. Heng TS, Painter MW. Immunological Genome Project C. The Immunological Genome Project: networks of gene expression in immune cells. Nat Immunol. 2008;9:1091–4.
52. Benayoun BA, Pollina EA, Singh PP, Mahmoudi S, Harel I, Casey KM, et al. Remodeling of epigenome and transcriptome landscapes with aging in mice reveals widespread induction of inflammatory responses. Genome Res. 2019; 29:697–709.
53. Han X, Wang R, Zhou Y, Fei L, Sun H, Lai S, et al. Mapping the mouse. Cell Atlas Microwell-Seq Cell. 2018;172:1091–107.e1017.
54. Martens JH, Stunnenberg HG. BLUEPRINT: mapping human blood cell epigenomes. Haematologica. 2013;98:1487–9.
55. de Souza N. The ENCODE project. Nat Methods. 2012;9:1046.
56. Mabbott NA, Baillie JK, Brown H, Freeman TC, Hume DA. An expression atlas of human primary cells: inference of gene function from coexpression networks. BMC Genomics. 2013;14:632.
57. Monaco G, Lee B, Xu W, Mustafah S, Hwang YY, Carre C, et al. RNA-Seq signatures normalized by mRNA abundance allow absolute deconvolution of human immune cell types. Cell Rep. 2019;26:1627–40.e1627.
58. Korotkevich G, Sukhov V, Budin N, Shpak B, Artyomov MN, Sergushichev A. Fast gene set enrichment analysis. bioRxiv: 060012 [Preprint]. 2021. Available from: https://doi.org/10.1101/060012.
59. Subramanian A, Tamayo P, Mootha VK, Mukherjee S, Ebert BL, Gillette MA, et al. Gene set enrichment analysis: a knowledge-based approach for interpreting genome-wide expression profiles. Proc Natl Acad Sci USA. 2005;102:15545–50.
60. Hanzelmann S, Castelo R, Guinney J. GSVA: gene set variation analysis for microarray and RNA-seq data. BMC Bioinforma. 2013;14:7.
61. Love MI, Huber W, Anders S. Moderated estimation of fold change and dispersion for RNA-seq data with DESeq2. Genome Biol. 2014;15:550.
62. Liberzon A, Birger C, Thorvaldsdottir H, Ghandi M, Mesirov JP, Tamayo P. The Molecular Signatures Database (MSigDB) hallmark gene set collection. Cell Syst. 2015;1:417–25.
63. Wickham H. ggplot2: elegant graphics for data analysis. *Use R!* 2nd ed. Cham: Springer International Publishing: Imprint: Springer; 2016. pp. 1.
64. Roulston A, Marcellus RC, Branton PE. Viruses and apoptosis. Annu Rev Microbiol. 1999;53:577–628.
65. Saito K, Meyer K, Warner R, Basu A, Ray RB, Ray R. Hepatitis C virus core protein inhibits tumor necrosis factor alpha-mediated apoptosis by a protective effect involving cellular FLICE inhibitory protein. J Virol. 2006;80:4372–9.
66. Lee AR, Lim KH, Park ES, Kim DH, Park YK, Park S, et al. Multiple functions of cellular FLIP are essential for replication of hepatitis B virus. J Virol 2018;92:1–19.
67. Krueger A, Fas SC, Giaisi M, Bleumink M, Merling A, Stumpf C, et al. HTLV-1 Tax protects against CD95-mediated apoptosis by induction of the cellular FLICE-inhibitory protein (c-FLIP). Blood. 2006;107:3933–9.
68. Gibellini D, Re MC, Ponti C, Vitone F, Bon I, Fabbri G, et al. HIV-1 Tat protein concomitantly down-regulates apical caspase-10 and up-regulates c-FLIP in lymphoid T cells: a potential molecular mechanism to escape TRAIL cytotoxicity. J Cell Physiol. 2005;203:547–56.
69. Tepper CG, Seldin MF. Modulation of caspase-8 and FLICE-inhibitory protein expression as a potential mechanism of Epstein-Barr virus tumorigenesis in Burkitt's lymphoma. Blood. 1999;94:1727–37.
70. Rodrigue-Gervais IG, Labbé K, Dagenais M, Dupaul-Chicoine J, Champagne C, Morizot A, et al. Cellular inhibitor of apoptosis protein cIAP2 protects against pulmonary tissue necrosis during influenza virus infection to promote host survival. Cell Host Microbe. 2014;15:23–35.
71. Nienhold R, Ciani Y, Koelzer VH, Tzankov A, Haslbauer JD, Menter T, et al. Two distinct immunopathological profiles in autopsy lungs of COVID-19. Nat Commun. 2020;11:5086.
72. Rossi G, Cavazza A, Spagnolo P, Bellafiore S, Kuhn E, Carassai P, et al. The role of macrophages in interstitial lung diseases: Number 3 in the Series "Pathology for the clinician" Edited by Peter Dorfmuller and Alberto Cavazza. Eur Respir Rev. 2017;26:1–16.
73. Duan M, Hibbs ML, Chen W. The contributions of lung macrophage and monocyte heterogeneity to influenza pathogenesis. Immunol Cell Biol. 2017;95:225–35.
74. Matsuyama T, Kubli SP, Yoshinaga SK, Pfeffer K, Mak TW. An aberrant STAT pathway is central to COVID-19. Cell Death Differ. 2020;27:3209–25.
75. Trovato R, Fiore A, Sartori S, Canè S, Giugno R, Cascione L, et al. Immunosuppression by monocytic myeloid-derived suppressor cells in patients with pancreatic ductal carcinoma is orchestrated by STAT3. J Immunother Cancer. 2019;7:255.

76. Ugel S, Cane S, De Sanctis F, Bronte V. Monocytes in the tumor microenvironment. Annu Rev Pathol. 2021;16:93–122.
77. Vasquez-Dunddel D, Pan F, Zeng Q, Gorbounov M, Albesiano E, Fu J, et al. STAT3 regulates arginase-I in myeloid-derived suppressor cells from cancer patients. J Clin Invest. 2013;123:1580–9.
78. Yu H, Pardoll D, Jove R. STATs in cancer inflammation and immunity: a leading role for STAT3. Nat Rev Cancer. 2009;9:798–809.
79. Merad M, Martin JC. Pathological inflammation in patients with COVID-19: a key role for monocytes and macrophages. Nat Rev Immunol. 2020;20:355–62.
80. Bronte V, Ugel S, Tinazzi E, Vella A, De Sanctis F, Canè S, et al. Baricitinib restrains the immune dysregulation in patients with severe COVID-19. J Clin Invest. 2020;130:6409–16.
81. Jiang RD, Liu MQ, Chen Y, Shan C, Zhou YW, Shen XR, et al. Pathogenesis of SARS-CoV-2 in transgenic mice expressing human angiotensin-converting enzyme 2. Cell. 2020;182:50–8.e58.
82. Veras FP, Pontelli MC, Silva CM, Toller-Kawahisa JE, de Lima M, Nascimento DC, et al. SARS-CoV-2-triggered neutrophil extracellular traps mediate COVID-19 pathology. J Exp Med. 2020;217:1–12.
83. Hallahan DE, Staba-Hogan MJ, Virudachalam S, Kolchinsky A. X-ray-induced P-selectin localization to the lumen of tumor blood vessels. Cancer Res. 1998;58:5216–20.
84. Middleton EA, He XY, Denorme F, Campbell RA, Ng D, Salvatore SP, et al. Neutrophil extracellular traps contribute to immunothrombosis in COVID-19 acute respiratory distress syndrome. Blood. 2020;136:1169–79.
85. Brinkmann V, Reichard U, Goosmann C, Fauler B, Uhlemann Y, Weiss DS, et al. Neutrophil extracellular traps kill bacteria. Science. 2004;303:1532–5.
86. Keshari RS, Jyoti A, Dubey M, Kothari N, Kohli M, Bogra J, et al. Cytokines induced neutrophil extracellular traps formation: implication for the inflammatory disease condition. PLoS ONE. 2012;7:e48111.
87. Thome M, Tschopp J. Regulation of lymphocyte proliferation and death by FLIP. Nat Rev Immunol. 2001;1:50–8.
88. Winkler ES, Bailey AL, Kafai NM, Nair S, McCune BT, Yu J, et al. SARS-CoV-2 infection of human ACE2-transgenic mice causes severe lung inflammation and impaired function. Nat Immunol. 2020;21:1327–35.
89. Hoang TN, Pino M, Boddapati AK, Viox EG, Starke CE, Upadhyay AA, et al. Baricitinib treatment resolves lower-airway macrophage inflammation and neutrophil recruitment in SARS-CoV-2-infected rhesus macaques. Cell 2020; 184:460–75.
90. Zilionis R, Engblom C, Pfirschke C, Savova V, Zemmour D, Saatcioglu HD, et al. Single-cell transcriptomics of human and mouse lung cancers reveals conserved myeloid populations across individuals and species. Immunity. 2019;50:1317–34.
91. Verdura S, Cuyàs E, Llorach-Parés L, Pérez-Sánchez A, Micol V, Nonell-Canals A, et al. Silibinin is a direct inhibitor of STAT3. Food Chem Toxicol. 2018;116: 161–72.
92. O'Shea JJ, Holland SM, Staudt LM. JAKs and STATs in immunity, immunodeficiency, and cancer. N Engl J Med. 2013;368:161–70.
93. Ruder B, Murtadak V, Stürzl M, Wirtz S, Distler U, Tenzer S, et al. Chronic intestinal inflammation in mice expressing viral Flip in epithelial cells. Mucosal Immunol. 2018;11:1621–9.
94. Ballon G, Chen K, Perez R, Tam W, Cesarman E. Kaposi sarcoma herpesvirus (KSHV) vFLIP oncoprotein induces B cell transdifferentiation and tumorigenesis in mice. J Clin Invest. 2011;121:1141–53.
95. Karki R, Sharma BR, Tuladhar S, Williams EP, Zalduondo L, Samir P, et al. Synergism of TNF-α and IFN-γ triggers inflammatory cell death, tissue damage, and mortality in SARS-CoV-2 infection and cytokine shock syndromes. Cell 2021; 184:149–68.e17.
96. Park SJ, Sohn HY, Yoon J, Park SI. Down-regulation of FoxO-dependent c-FLIP expression mediates TRAIL-induced apoptosis in activated hepatic stellate cells. Cell Signal. 2009;21:1495–503.
97. Sun J, Ye F, Wu A, Yang R, Pan M, Sheng J, et al. Comparative transcriptome analysis reveals the intensive early stage responses of host cells to SARS-CoV-2 infection. Front Microbiol. 2020;11:1–12.
98. Safa AR. Roles of c-FLIP in apoptosis, necroptosis, and autophagy. J Carcinog Mutagen. 2013;Suppl 6:003.
99. Adamo A, Frusteri C, Pallotta MT, Pirali T, Sartoris S, Ugel S. Moonlighting proteins are important players in cancer immunology. Front Immunol. 2020;11: 613069.
100. Murakami M, Harada M, Kamimura D, Ogura H, Okuyama Y, Kumai N, et al. Disease-association analysis of an inflammation-related feedback loop. Cell Rep. 2013;3:946–59.
101. Hirano T, Murakami M. COVID-19: a new virus, but a familiar receptor and cytokine release syndrome. Immunity. 2020;52:731–3.
102. Nie X, Qian L, Sun R, Huang B, Dong X, Xiao Q, et al. Multi-organ proteomic landscape of COVID-19 autopsies. Cell. 2021;184:775–91.e714.
103. Stebbing J, Sánchez Nievas G, Falcone M, Youhanna S, Richardson P, Ottaviani S, et al. JAK inhibition reduces SARS-CoV-2 liver infectivity and modulates inflammatory responses to reduce morbidity and mortality. Sci Adv. 2020;7:1–15.
104. Kalil AC, Patterson TF, Mehta AK, Tomashek KM, Wolfe CR, Ghazaryan V, et al. Baricitinib plus remdesivir for hospitalized adults with Covid-19. N Engl J Med. 2021;384:795–807.
105. Food and Drug Administration Report. Frequently asked questions on the Emergency Use Authorization of baricitinib for treatment of COVID-19. Accessed 29 Jul 2021.
106. Qing Y, Stark GR. Alternative activation of STAT1 and STAT3 in response to interferon-gamma. J Biol Chem. 2004;279:41679–85.
107. Murray PJ. The JAK-STAT signaling pathway: input and output integration. J Immunol. 2007;178:2623–9.

ACKNOWLEDGEMENTS

We thank Silvia Sartoris, Rosalinda Trovato, Varvara Petrova, Laura Pinton, Monica Castellucci, Tommaso Grandi, and Gianmarco Tarquini for their support and helpful discussion during the development of this research. We thank Giulio Fracasso, Ornella Poffe, Cristina Anselmi and Tiziana Cestari for perfect technical assistance. We thank Pierre Bost, David Eyal, Jimmy Caroli, Oriana Romano, and Mattia Forcato for bioinformatics support. We deeply acknowledge the contribution of 'Centro Piattaforme Tecnologiche' of the University of Verona for sorting and imaging experiments and 'Centro Interdipartimentale di Servizio alla Ricerca Sperimentale' of the University of Verona for maintaining mouse colonies. We thank Ethel Cesarman (Weill Cornell Medical College, New York, NY, USA) for the gift of the Rosa26.vFLIP conditional allele mice. We also thank all the personnel involved in the patients' care and assistance; in particular, we thank Sara Boschetti, Francesca Del Favero, Riccardo Boetti, Pasquale De Nardo, Fabiana Busti, Chiara Mozzin, Federica Marola, and Valentina Albanese. We wish to thank all the members of the Immunology section of Department of Medicine of University of Verona who worked forcefully during pandemic. The authors wish to thank Servier Medical Art templates for the artwork used in the figures of this manuscript, which are licensed under a Creative Common Attribution 3.0 Unported License; https://smart.servier.com. Finally, we dedicate this work to the memory of the health care workers who have given their lives in the care of patients with COVID-19.

AUTHOR CONTRIBUTIONS

C.M., Si.C., A.F., V.B. and S.U. conceptualized the study; C.M., Si.C., A.F. and S.U. designed the methodology; C.M., Si.C., A.F., C.F., F.D.S., St.C., A.A., F.H., R.M.B. and S.U. performed experiments and revised the manuscript; A.L., F.D.P. and M.I. conducted the immunohistochemistry and pathology analysis, interpreted data, and revised the manuscript; Si.C., A.G. and S.B. conducted computational analysis, interpreted data, and revised the manuscript; S.Z. and P.S. co-designed the in vivo RNA delivery experiments, interpreted data, and revised the manuscript; E.T., K.D., L.G., E.P., D.G., I.P., P.A.I., D.A. and A.C. were responsible for biological specimens and patients' data collection and revised the manuscript; Y.C. and Z.L.S. developed methodology of human ACE2 mouse model, performed pathological analysis, interpreted data, and revised the manuscript; P.J.M. contributed to writing the paper and revised the manuscript; M.C. interpreted data; I.A. co-designed the study, interpreted data, contributed to writing the paper, and revised the manuscript; V.B. and S.U. directed the project, designed the study, interpreted data, supervised research, wrote the manuscript, and acquired the funding.

FUNDING

This work was jointly supported by both S. Ugel grants of the Fondazione Italian Association for Cancer Research (AIRC, MFAG project: 21509) and PRIN program of Italian Ministry of Education, University and Research (MIUR, CUP: B38D19000140006) and V. Bronte grants funded by Fondazione Cariverona (ENACT Project), Fondazione TIM (Immunovid Project), Fondazione AIRC (23788), Cancer Research Institute (Clinic and Laboratory Integration Program, CLIP 2020), European Research Commission (Euronanomed III, Joint Translational Call_2017, Project RESOLVE), and MIUR (CUP: B38D19000260006).

COMPETING INTERESTS

A.F., S.U., and V.B. hold proprietary rights on the patent applications about engineered cells for inducing tolerance by BioNTech (Mainz, Germany). S.Z., V.B., and P.S. hold proprietary rights on the patent applications about 4PD technology by the University of Miami (Miami, USA). No potential conflicts of interest were disclosed by the other authors.

ETHIC STATEMENT

Our studies include human participants, human data, or human tissues. All the patients (and/or initially their families) provided written informed consent before sampling and for the use of their clinical and biological data. This study was approved by the local ethical committee (protocol 17963; PI: Vincenzo Bronte; ClinicalTrials.gov identifier NCT04438629). All clinical investigations were conducted according to the Declaration of Helsinki principles, and informed consent was obtained from all study participants. Animal experiments were performed according to national (protocol number C46F4.26 approved by the Ministerial Decree Number 993/2020-PR of July 24, 2020 [PI: Stefano Ugel] and protocol number C46F4.8 approved by the Ministerial Decree Number 207/2018-PR of February 21, 2018 [PI: Vincenzo Bronte]) and European laws and regulations. All animal experiments were approved by Verona University Ethical Committee and conducted according to the guidelines of Federation of European Laboratory Animal Science Association (FELASA).

ADDITIONAL INFORMATION

Supplementary information The online version contains supplementary material available at https://doi.org/10.1038/s41418-021-00866-0.

Correspondence and requests for materials should be addressed to Vincenzo Bronte or Stefano Ugel.

SUPPLEMENTAL INFORMATION

Supplemental Figures

- Fig. S1. Clinical characteristic of enrolled patients and immunosuppressive function of monocytes.
- Fig. S2. vFLIP chimera mice develop cytokine release syndrome.
- Fig. S3. Systemic and local features of cytokine release syndrome in vFLIP mice.
- Fig. S4. Single-cell transcriptional profiling of lung-infiltrating cells in vFLIP mice and BAL-derived immune cells obtained from COVID-19 patients.
- Fig. S5. Characterization of the pharmacological STAT3-targeting effectiveness in vFLIP mice.
- Fig. S6. Characterization of the in vivo STAT3-silencing effectiveness in vFLIP mice.
- Dataset 1. scRNA-seq data and statistics.

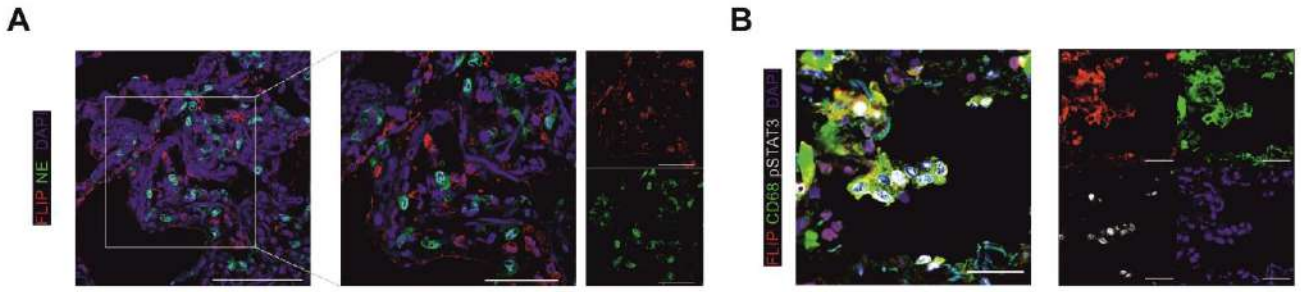

C

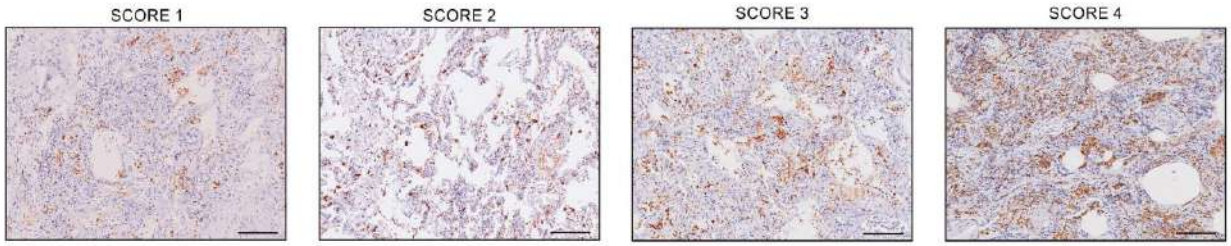

Positivity for CD68/FLIP/STAT3	Hospitalization days	CD68 score
No	27.2 ±14.37	2.1 ± 0.8
Yes	15 ± 9.3	2.2 ± 1.0

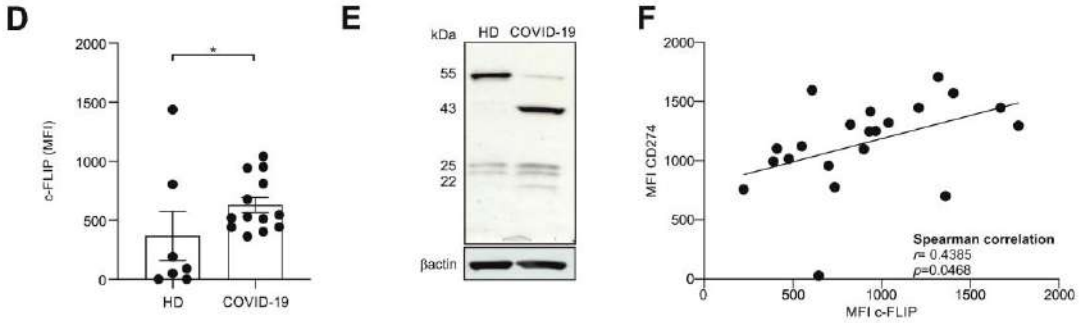

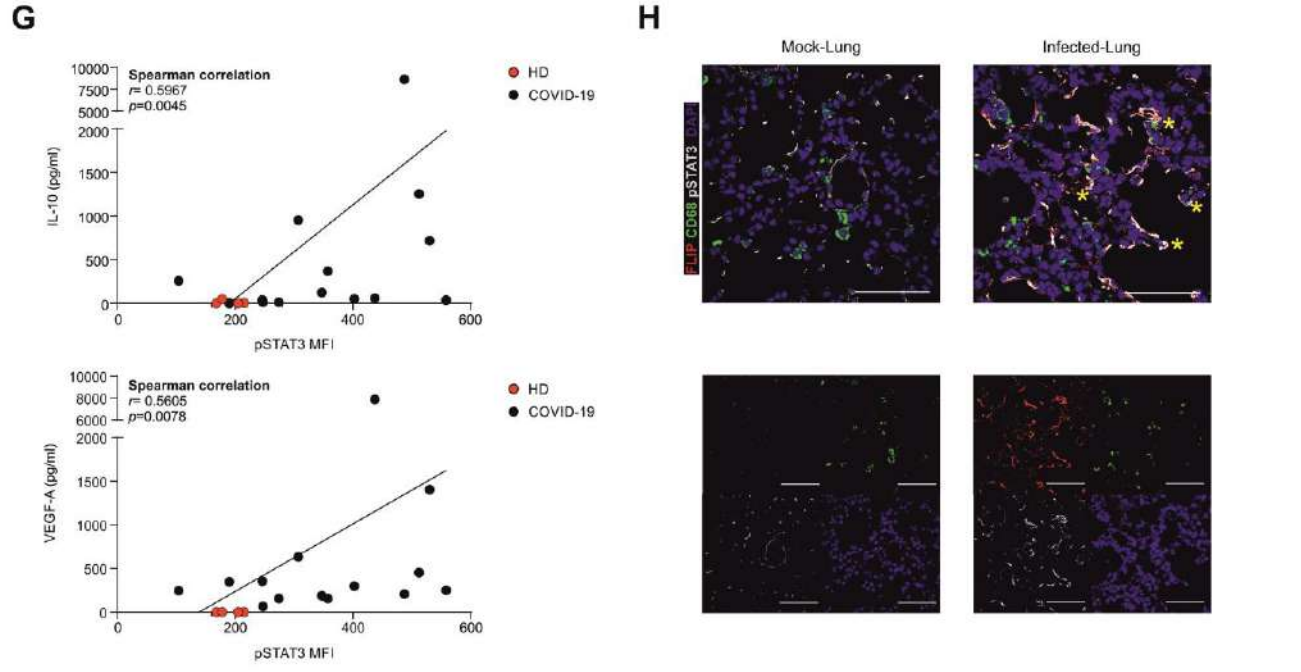

Fig. S1. Clinical features of enrolled patients and immunosuppressive function of monocytes and CD68$^+$ cells in lung of hACE2 infected mice.

A Representative immunofluorescence (IF) staining of lung-infiltrating neutrophils (NE$^+$ cells) in COVID-19 patients. Cells were stained for NE (green), FLIP (red) and DAPI (blue). Scale bar, 50 μm. **B** Representative immunofluorescence (IF) staining of monocytes (CD68$^+$ cells) of COVID-19 patient. Cells were stained for CD68 (green), c-FLIP (red), pSTAT3 (white) and DAPI (blue). Scale bar, 20 μm. **C** CD68$^+$ cells infiltration in lung samples (n=23) of the enrolled COVID-19 patient's cohort was defined using an arbitrary scoring from 1 to 4. Representative IHC images used to define CD68 score. The score of CD68-expressing cells does not discriminate between patients with a shorter (15±9.3 days) or a longer (27.2±14.37 days) hospitalization time. **D** FLIP expression in circulating monocytes (CD14$^+$ cells) purified from health donor (HD, n=7) or COVID-19 patients (n=13). **E** Western blot analysis for FLIP expression ($FLIP_L$, p43, $FLIP_S$ and p21) on circulating monocytes (CD14$^+$ cells) isolated from HD or COVID-19 patients. **F** Correlation between CD274 (PD-L1) and c-FLIP expression in COVID-19 circulating monocytes (CD14$^+$ cells) (n=19). **G** Correlation between the release of IL-10 or VEGF-A cytokines and pSTAT3 expression in circulating monocytes (CD14$^+$ cells) from HD (red, n=4) and COVID-19 patients (black, n=13). **H** Representative indirect immunofluorescence (IFA) staining of FLIP (red), CD68 (green), pSTAT3 (white) and DAPI (blue) in lungs of HFH4-hACE2 transgenic mice SARS-CoV-2-infected or mock-infected. Scale bar, 60μm. Correlation analysis was performed by Spearman's rank correlation (**F**, **G**). Data are reported as mean ± S.E.M. *$p \leq 0.05$, **$p \leq 0.01$ and ***$p \leq 0.001$ by Mann–Whitney test (**D**).

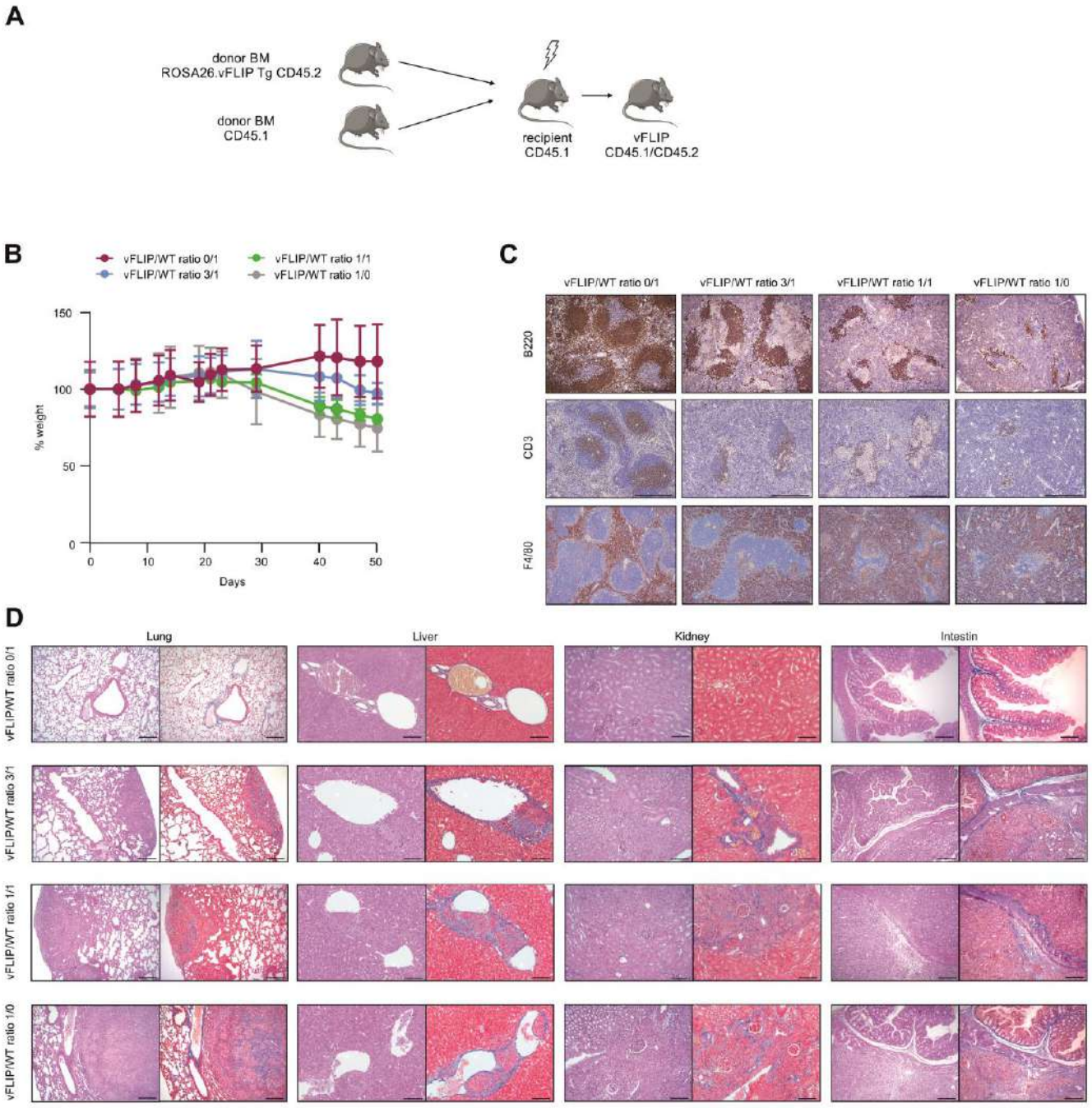
A
donor BM
ROSA26.vFLIP Tg CD45.2
donor BM
CD45.1
recipient
CD45.1
vFLIP
CD45.1/CD45.2
B
vFLIP/WT ratio 0/1
vFLIP/WT ratio 3/1
vFLIP/WT ratio 1/1
vFLIP/WT ratio 1/0
% weight
Days
C
B220
CD3
F4/80
D
Lung
Liver
Kidney
Intestin

Fig. S2. vFLIP chimera mice develop cytokine release syndrome.
A Experimental layout of chimera (vFLIP) mice generation. **B** Variation of body weight during CRS progression in vFLIP chimera mice (n=3, for each condition). **C** IHC analysis of spleen in vFLIP mice: lymphocytes ($B220^+$ cells: B lymphocytes; $CD3^+$ cells: T lymphocytes) and mononuclear phagocytes ($F4/80^+$ cells). Scale bar, 400 μm. **D** Representative H&E-stained microscopy images and Masson's Trichrome of lung, liver, kidney and intestine of vFLIP mice. Scale bar, 100 μm.

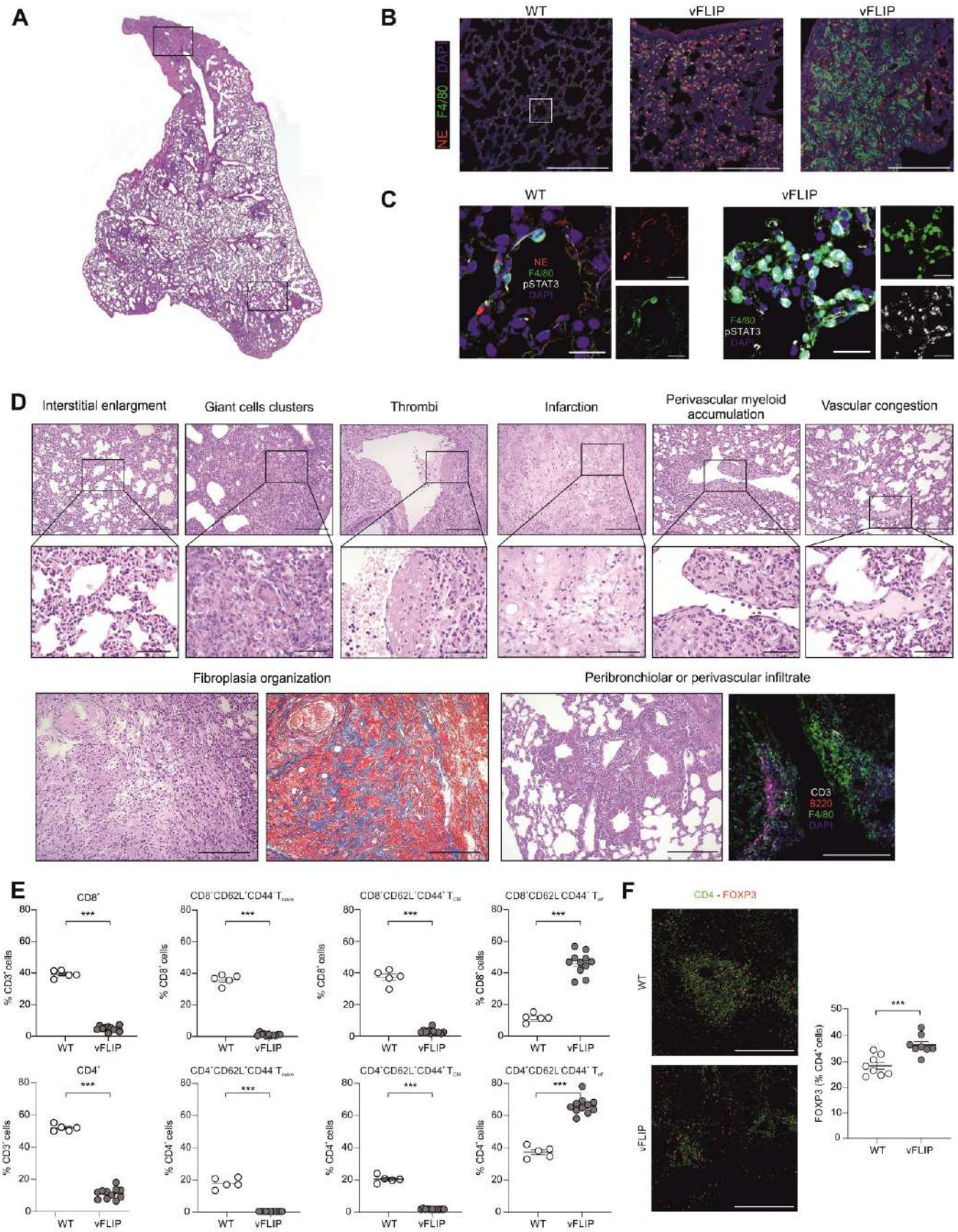
A
B
WT
vFLIP
vFLIP
NE F4/80 DAPI
C
WT
vFLIP
NE
F4/80
pSTAT3
DAPI
F4/80
pSTAT3
DAPI
D
Interstitial enlargment
Giant cells clusters
Thrombi
Infarction
Perivascular myeloid accumulation
Vascular congestion
Fibroplasia organization
Peribronchiolar or perivascular infiltrate
CD3
B220
F4/80
DAPI
E
CD8+
CD8+CD62L-CD44+ TN/M
CD8+CD62L-CD44+ TCM
CD8+CD62L-CD44+ TEF
CD4+
CD4+CD62L-CD44+ TN/M
CD4+CD62L-CD44+ TCM
CD4+CD62L-CD44+ TEF
% CD3+ cells
% CD8+ cells
% CD4+ cells
***
WT
vFLIP
F
CD4 - FOXP3
WT
vFLIP
FOXP3 (% CD4+ cells)
***

Fig. S3. Systemic and local features of cytokine release syndrome in vFLIP mice.

A Representative H&E-stained microscopy of lung tissue of vFLIP mice. **B** Representative IF staining of lung-infiltrating neutrophils (NE^+ cells) and mononuclear phagocytes ($F4/80^+$ cells) in WT or vFLIP mice. Cells were stained for DAPI (blue), neutrophil elastase (NE) (red, middle panel) and F4/80 (green, right panel). Scale bar, 200 µm. **C** Representative IF staining of lung-infiltrating neutrophils (NE^+ cells) and mononuclear phagocytes ($F4/80^+$ cells) in WT or vFLIP mice. Scale bar, 20 µm. Cells were stained for DAPI (blue), NE (red) or F4/80 (green) and pSTAT3 Tyr705 (grey). **D** Representative H&E-stained microscopy images of pathological score: interstitial enlargement, giant cells clusters, thrombi, infarction, perivascular myeloid accumulation, vascular congestion, fibroplasia organization and peribronchiolar or perivascular infiltrate vFLIP mice. Scale bar, 200 µm (upper panel) and 50 µm (bottom panel). **E** Flow cytometry analysis of $CD3^+$ T cell subsets in the spleen of vFLIP mice (n=11) and WT mice (n=5). Lymphocytes were segregated into $T_{effector}$ ($CD62L^-CD44^+$), T_{naive} ($CD62L^+CD44^-$) and $T_{central\ memory}$ ($CD62L^+CD44^+$). **F** Representative IF staining of $CD4^+$ $FOXP3^+$ cells in spleen of vFLIP mice (n=8) and WT (n=8). Data are reported as mean ± S.E.M. *$p \leq 0.05$, **$p \leq 0.01$ and ***$p \leq 0.001$ by Mann–Whitney test (**E**, **F**).


A
scRNA-Seq
(Lung)
tSNE 2
31,274
tSNE 1
Neutrophils
Macrophages
B cells
Monocytes
T cells
NK cells
DC
ILC
Fibroblasts
Epithelial cells
Endothelial cells
Erythroblasts/Erythrocytes
Basophils
Mast cells
Unclassified
100%
75%
50%
25%
0%
WT 1
WT 2
vFLIP 1
vFLIP 2
Chimera UT
Chimera silibinin
Chimera baricitinib
B
Mast cells
Basophils
Erythroblasts/Erythrocytes
Endothelial cells
Epithelial cells
Fibroblasts
ILC
DC
NK cells
T cells
Monocytes
B cells
Macrophages
Neutrophils
Ptprc
Cd68
Ear2
Ly6c2
Csf1r
Batf3
Fscn1
Ccr7
S100a8
S100a9
Csf3r
Cd79a
Fcnr
Cd19
Cd3d
Cd3e
Il7r
Gzma
Klrb1c
Nkg7
Hba-a1
Hba-a2
Glypa
Gata2
Cpa3
Ms4a2
Epcam
Krt8
Krt18
Col3a1
Col1a2
Col1a1
Pecam1
Mcam
Vwf
Average expression
2
1
0
Percent expressed
0
25
50
75
100
C
scRNA-Seq
(COVID-19
BAL)
tSNE 2
19,996
tSNE 1
Neutrophils
Macrophages
Monocytes
T cells
Epithelial cells
Erythroblasts/Erythrocytes
NK cells
DC
Unclassified
100%
75%
50%
25%
0%
BAL16
BAL3
BAL29
BAL7
BAL24
BAL25
BAL10
D
DC
NK cells
Erythroblasts/Erythrocytes
Epithelial cells
T cells
Monocytes
Macrophages
Neutrophils
PTPRC
CD68
CD14
VCAN
CSF1R
CSF3R
FCGR3B
CD80
CCR7
CD3D
CD3E
KLRD1
NKG7
EPCAM
KRT18
HBA1
HBA2
Average expression
2
1
0
Percent expressed
0
25
50
75
100

Fig. S4. Single-cell transcriptional profiling of lung-infiltrating cells in vFLIP mice and BAL-derived immune cells obtained from COVID-19 patients.
A tSNE representation of scRNA-seq from all mouse samples (31,274 cells) colored according to cell type. Stacked bar plots representing cell type proportions across all the mouse samples. **B** Dot plot showing the scaled average expression of known marker genes for the mouse cell populations identified. **C** tSNE representation of scRNA-seq from fatal COVID-19 BALs patients (19,996) colored according to cell type. Stacked bar plots representing cell type proportions across all the human BAL samples. **D** Dot plot showing the scaled average expression of known marker genes for the cell types identified in the BALs.

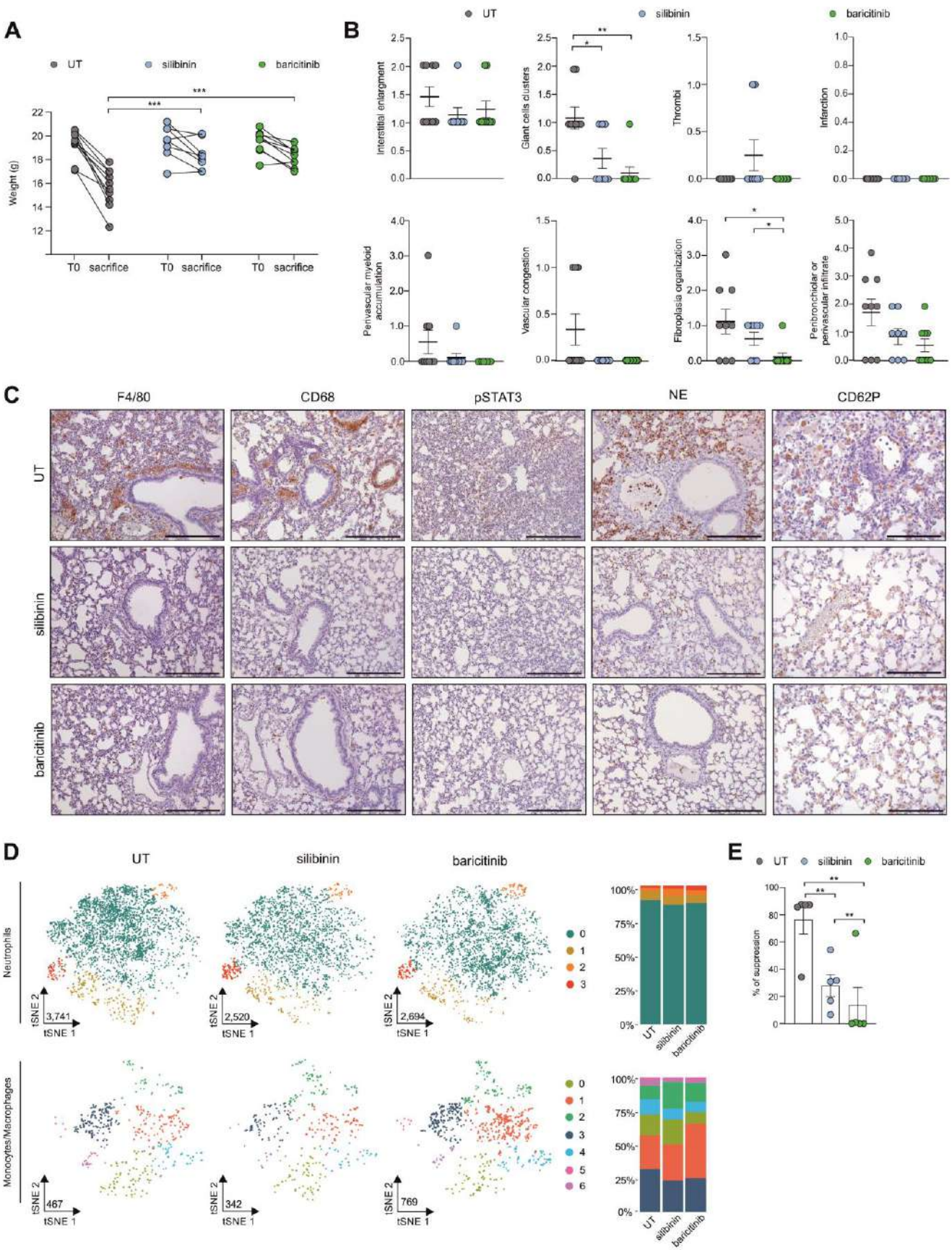
A
UT
silibinin
baricitinib
Weight (g)
T0 sacrifice
T0 sacrifice
T0 sacrifice
B
UT
silibinin
baricitinib
Interstitial enlargment
Giant cells clusters
Thrombi
Infarction
Perivascular myeloid accumulation
Vascular congestion
Fibroplasia organization
Peribronchiolar or perivascular infiltrate
C
F4/80
CD68
pSTAT3
NE
CD62P
UT
silibinin
baricitinib
D
UT
silibinin
baricitinib
Neutrophils
Monocytes/Macrophages
tSNE 2
tSNE 1
3,741
2,520
2,694
467
342
769
0
1
2
3
4
5
6
100%
75%
50%
25%
0%
UT
silibinin
baricitinib
E
UT
silibinin
baricitinib
% of suppression

Fig. S5. Characterization of the pharmacological STAT3-targeting effectiveness in vFLIP mice.

A Body weights of vFLIP chimera mice before treatment (T0) or at the end of treatment (untreated, n=9; silibinin, n=8; baricitinib, n=9). **B** Dot plots of pathological score parameters: interstitial enlargement, giant cells clusters, thrombi, infarction, perivascular myeloid accumulation, vascular congestion, fibroplasia organization and peribronchiolar or perivascular infiltrate (untreated, n=9; silibinin, n=8; baricitinib, n=9). **C** Representative IHC images of F4/80, CD68, p-STAT3, NE and CD62P in lungs isolated from vFLIP mice untreated or treated with either silibinin or baricitinib. Scale bar, 200 µm. **D** tSNE representation of neutrophil subsets across untreated (3,741) mice and treated with silibinin (2,520) and baricitinib (2,694) colored according to cluster analysis (top). Stacked bar plots representing neutrophil clusters proportions across conditions. tSNE representation of monocytes/macrophages subsets across untreated (467) mice and treated with silibinin (342) and baricitinib (769) colored according to cluster analysis (bottom). Stacked bar plots representing monocytes/macrophages cluster proportions across conditions. **E** Functional assay performed at 1:3 ratio of PBMCs:CD14+ cells using purified monocytes from COVID-19 patients (n = 5) treated with silibinin (200µm), baricitinib (200µm) or left untreated. Data are reported as mean ± S.E.M. *$p \leq 0.05$, **$p \leq 0.01$ and ***$p \leq 0.001$ by Mann–Whitney test (A,B,E).

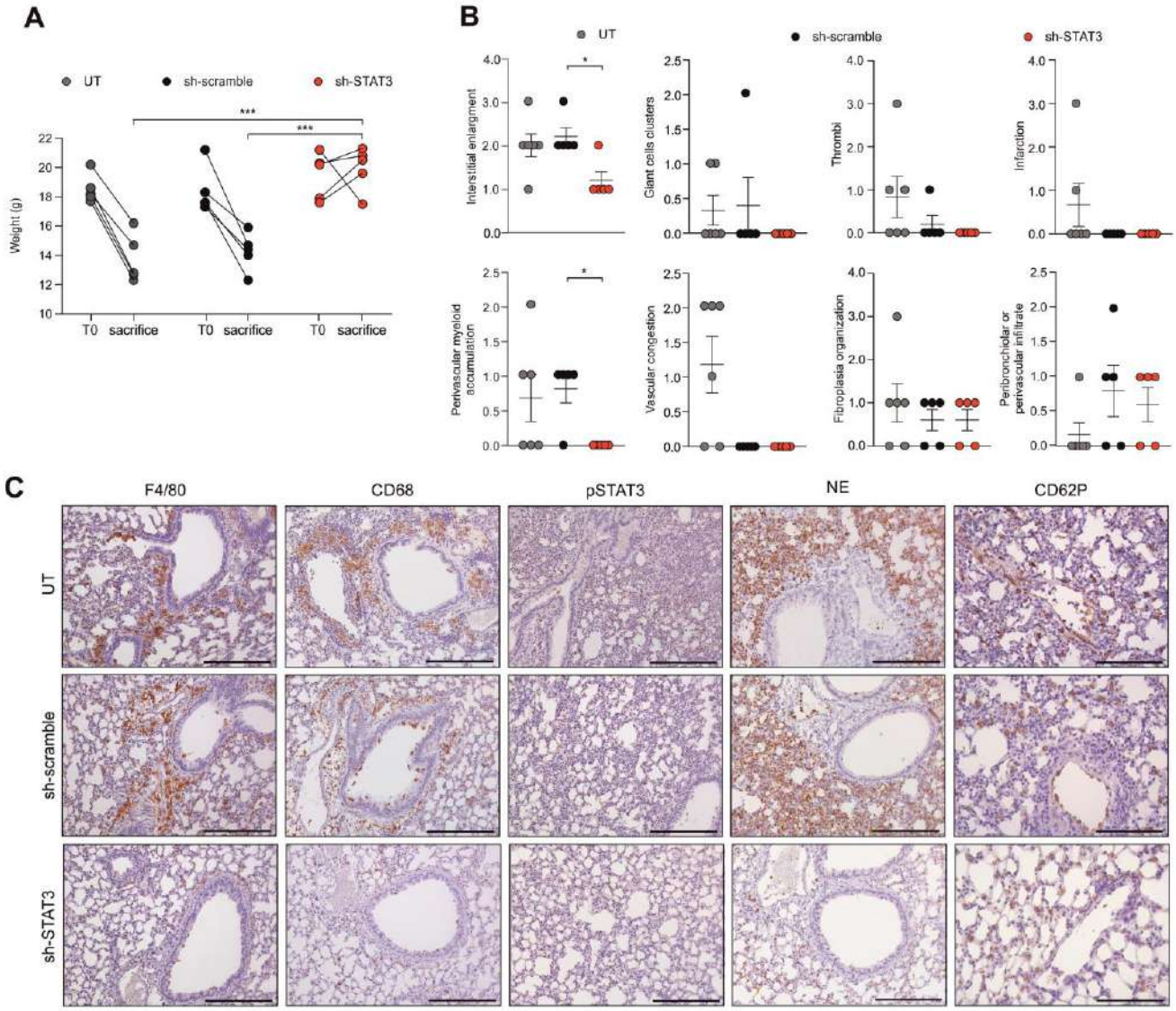
A
UT
sh-scramble
sh-STAT3
***
***
Weight (g)
T0 sacrifice
T0 sacrifice
T0 sacrifice
B
UT
sh-scramble
sh-STAT3
Interstitial enlargment
Giant cells clusters
Thrombi
Infarction
Perivascular myeloid accumulation
Vascular congestion
Fibroplasia organization
Peribronchiolar or perivascular infiltrate
C
F4/80
CD68
pSTAT3
NE
CD62P
UT
sh-scramble
sh-STAT3

Fig. S6. Characterization of the in vivo STAT3-silencing effectiveness in vFLIP mice.

A Body weights of vFLIP chimera mice before treatment (T0) or at the end of treatment (untreated, n=6; sh-scramble, n=5; sh-STAT3, n=5). **B** Dot plots of pathological score parameters: interstitial enlargement, giant cells clusters, thrombi, infarction, perivascular myeloid accumulation, vascular congestion, fibroplasia organization and peribronchiolar or perivascular infiltrate (untreated, n=6; sh-scramble, n=5; sh-STAT3, n=5). **C** Representative IHC images of F4/80, CD68, p-STAT3, NE and CD62P in lungs isolated from vFLIP mice untreated or treated with either sh-STAT3 or sh-scramble. Scale bar, 200 μm. Data are reported as mean ± S.E.M. *$p \leq 0.05$, **$p \leq 0.01$ and ***$p \leq 0.001$ by Mann–Whitney test.